JOURNAL OF AIRCRAFT
Vol. 47, No. 3, May–June 2010

Small Disturbance Navier–Stokes Computations for Low-Aspect-Ratio Wing Pitching Oscillations

Alexander Pechloff* and Boris Laschka†
Technical University of Munich, 85748 Garching, Germany

DOI: 10.2514/1.45233

For dynamic production aeroelastic analysis in the transonic speed range, a computational fluid dynamics method based on the small disturbance Navier–Stokes equations can serve as a reasonable alternative to one realizing the Reynolds-averaged Navier–Stokes equations' time-domain solution. Its dynamically linear approach promises a significantly decreased computation cost in the prediction of unsteady aerodynamic loading while retaining the latter's fidelity to a high degree. In this regard, research conducted at the Technical University of Munich has resulted in the computational fluid dynamics method FLM-SD.NS. Further substantiating its application readiness, harmonic pitching oscillations of the NASA clipped delta wing are investigated. Test cases are characterized by shocks of varying strengths and ranges of motion, as well as leading-edge vortex formation. Overall, results are in good agreement with dynamically fully nonlinear solutions provided by the comparative Reynolds-averaged Navier–Stokes solver FLM-NS, as well as available experimental data. Reductions in computation time, up to an order of magnitude, in relation to FLM-NS are observed. Limitations of the small disturbance approach, however, become apparent for the leading-edge vortex case, in which higher-order harmonics are far less negligible in the flow's response to the excitation.

Nomenclature

A	=	semispan planform area
AR	=	semispan aspect ratio, s^2/A
c	=	local chord length, $c(y/s)$
c_{av}	=	average chord length, A/s
c_L	=	lift coefficient, dimensional lift normalized with $\check{\rho}_\infty \lvert\check{\mathbf{v}}_\infty\rvert^2 \check{A}/2$
c_M	=	moment coefficient, dimensional moment respective to the pitch axis normalized with $\check{\rho}_\infty \lvert\check{\mathbf{v}}_\infty\rvert^2 \check{A}\check{c}_\mu/2$ (greater than 0: tail-heavy moment/pitch up)
c_p	=	pressure coefficient
$c_{p,\text{crit}}$	=	critical pressure coefficient, $c_p(Ma_\infty)$ at $Ma = 1.0$
c_r	=	root chord length, $c(0)$
c_t	=	tip chord length, $c(1)$
c_μ	=	reference chord length
d^+	=	sublayer-scaled distance of the first offbody grid plane
f	=	oscillation frequency
Im	=	imaginary part
k_{red}	=	reduced oscillation frequency
L	=	reference length of the geometric nondimensionalization
Ma	=	local Mach number
Ma_∞	=	freestream Mach number, $\lvert\check{\mathbf{v}}_\infty\rvert\sqrt{\check{\rho}_\infty}/\sqrt{\gamma\check{p}_\infty}$
p_∞	=	freestream static pressure
Pr	=	Prandtl number
Pr_t	=	turbulent Prandtl number
Re	=	real part
Re_∞	=	freestream Reynolds number, $\check{\rho}_\infty \lvert\check{\mathbf{v}}_\infty\rvert\check{c}_{\text{av}}/\check{\mu}_\infty$
s	=	semispan length
T_∞	=	freestream static temperature
t	=	time
$t_{\text{CPU}}^{\text{method}}$	=	Institute for Fluid Mechanics method computation time
$\lvert\mathbf{v}_\infty\rvert$	=	magnitude of the freestream velocity vector
x	=	span-station-local chordwise coordinate, $x(y/s)$ (0: leading edge, c: trailing edge)
x, y, z	=	global Cartesian coordinates
x_d	=	x of a wing section's maximum thickness
x_p, z_p	=	global pitch axis coordinates
y	=	semispan coordinate (0: root, s: tip)
α	=	incidence angle
γ	=	ratio of specific heats
Δ	=	difference between lower- and upper-surface values, $\Delta(x/c)$; for example, $\Delta c_p = c_{p,\text{lower}} - c_{p,\text{upper}}$
ζ_{CPU}	=	ratio of Institute for Fluid Mechanics method computation times, $\check{t}_{\text{CPU}}^{\text{NS}}/\check{t}_{\text{CPU}}^{\text{SD,NS}}$ or $\check{t}_{\text{CPU}}^{Eu}/\check{t}_{\text{CPU}}^{\text{SD}Eu}$
$\check{\varphi}_{\hat{\chi}}$	=	phase angle of $\hat{\chi}$, deg
λ	=	taper ratio, c_t/c_r
μ	=	molecular viscosity, governed by Sutherland's law
$\check{\mu}$	=	Spalart–Allmaras conservative working variable
μ_∞	=	freestream molecular viscosity, $\mu(T_\infty)$
ξ, η, ζ	=	curvilinear coordinates
ρ_∞	=	freestream density
τ_s	=	characteristic time, $\check{t}Ma_\infty\sqrt{\gamma\check{p}_\infty}/(\check{L}\sqrt{\check{\rho}_\infty})$
χ	=	generalized load coefficient, $\chi \in \{c_p, c_L, c_M\}$
$\lvert\hat{\chi}\rvert$	=	magnitude of $\hat{\chi}$, $\sqrt{(\text{Re}\hat{\chi})^2 + (\text{Im}\hat{\chi})^2}$

Superscripts

0	=	zeroth harmonic
1	=	first harmonic
2, 3	=	higher harmonics (second, third)
$\bar{}$	=	time-invariant mean
$\tilde{}$	=	periodic perturbation
$\hat{}$	=	perturbation amplitude
$\check{}$	=	dimensional

Received 1 May 2009; revision received 25 February 2010; accepted for publication 25 February 2010.

*Research Engineer, Institute for Aero- and Astronautics; alexander.pechloff@alumni.tum.de. Senior Member AIAA.

†Professor Emeritus, Institute for Aero- and Astronautics; Laschka@aer.mw.tum.de. Honorary Fellow AIAA.

Introduction

TO DATE, production analysis of an aircraft's dynamic aeroelastic behavior relies on low-order computational fluid dynamics (CFD) methods to supply the unsteady aerodynamic structural loading. This approach has proven to be highly efficient

and of excellent fidelity in the sub- and supersonic speed range. In the transonic speed range, however, which is the flight envelope's most critical respective instability (flutter), these methods fail to produce adequate predictions as convective nonlinearities, and viscous effects generally remain unaccounted for. A CFD method realizing the Reynolds-averaged Navier–Stokes (RANS) equations' time-domain solution, on the other hand, would be well suited to render the unsteady aerodynamic loading most accurately, as such flow properties are naturally inherent to the formulation. Unfortunately, even in the structurally uncoupled treatment, this type of high-order CFD method becomes computationally prohibitive when confronted with the multitude of parameter variations (Ma_∞, Re_∞, $\breve{\alpha}$, eigenmode, and k_{red}) required by the analysis [1]. Dual time-stepping schemes typically employed in the RANS equations' time-domain solution must sequentially realize a pseudosteady solution at each incremental deflection (physical time step) of the elastic body's neutral oscillatory motion. As the unsteady flowfield's periodicity is typically gained only after the computation of several oscillatory cycles, the aggregate number of pseudosteady solutions represents the primary cost, a circumstance which becomes especially expensive at low frequencies. A secondary cost rests in the accompanied incremental deformation of the body-embedding computational grid. For each physical time step, the computational grid must be updated to the body's new position, a task which becomes all the more expensive as the geometric complexity of the body increases. Lastly, the effort associated with the acquired data's postprocessing has to be taken into account. Since the unsteady loading is obtained as a series in time, subsequent Fourier analysis becomes necessary to extract the harmonics of interest. In doing so, turnaround time and thus throughput of the overall process is further diminished. Whereas the computational cost of this approach may be tolerable for an individual case, it becomes too high in the cumulation of production investigations.

Promising significantly decreased cost while yet retaining the fidelity of the RANS equations' time-domain solution to a high degree, a CFD method based on the small disturbance Navier–Stokes equations can serve as a reasonable alternative. For problems of dynamic stability, the elastic body's neutral oscillatory motion can be regarded as being limited to minor harmonic deflections about a reference position. Consequently, the organized unsteadiness inherent to the flowfield's instantaneous response can be presumed to be a predominantly dynamically linear perturbation about a time-invariant mean state. This would entail that higher-order harmonics present within the response become negligible to the point where a generally phase-shifted first harmonic prevails. Under the preceding assumption, a system of statistically treated linear partial differential equations exclusively governing the complex amplitude of the organized unsteadiness can be extracted from the instantaneous Navier–Stokes equations. With the elimination of time-dependency, time-accuracy and the accompanied incremental grid deformation are no longer an issue to the solution process. Thus, the necessary computational effort becomes comparable to the one involved with the steady-state solution of the RANS equations.

The small disturbance Navier–Stokes solution embodies magnitude and phase-shift of the organized unsteadiness. It develops contingent on a given oscillation frequency and amplitude surface deflection of the elastic body's harmonic motion, as well as the reference (time-invariant mean) flowfield about which the organized unsteadiness occurs. Common to both the small disturbance Navier–Stokes and the time-domain RANS method, the eigenmode-specific amplitude surface deflection yields from computational or experimental modal analysis, with the corresponding eigenfrequency gained as a by-product. The amplitude surface deflection is then numerically supplied by way of two computational grids. One embeds the elastic body at its reference position, while the other does so at its deflected extremum position. A steady-state RANS solution realized in the reference grid for the specific Ma_∞, Re_∞, $\breve{\alpha}$ serves as the time-invariant mean flowfield. For both an eigenmode and k_{red} variation, it remains unchanged. The further computation process of either method is depicted in Fig. 1.

The small disturbance approach handles dynamically nonlinear phenomena that would emerge in the flowfield's instantaneous response as dynamically linear perturbations about a statically nonlinear state, as contained in the time-invariant mean flowfield. This approximation, however, is sufficient to determine the linear stability of an aeroelastic system [2]. Contrary to the time-domain (dynamically fully nonlinear) approach, the unsteady loading is acquired directly. The obtained complex amplitude load represents the first-harmonic load resultant from the considered eigenmode's oscillation with k_{red}, while the afore computed time-invariant mean load embodies the zeroth-harmonic load. Naturally, the treatment of a body's elastic oscillations represents the most general case, the consideration of rigid oscillations for an a priori known frequency being equally feasible. In this instance, the amplitude surface deflection is replaced by the translational and/or rotational amplitude displacement. The benefits of the small disturbance approach over its dynamically fully nonlinear counterpart, valid for both the viscous and inviscid incarnation, are summarized in Table 1.

The small disturbance Navier–Stokes approach has its origin in the field of turbomachinery, where respective computational methods were developed to provide an accurate and efficient means of investigating unsteady viscous flow effects within a blade design environment. Also referred to as frequency-domain time-linearized Navier–Stokes methods, pioneering work has been conducted by Clark and Hall, who harnessed the approach for the analysis of stall flutter in two-dimensional cascades [3]. Since then, the dynamically linear treatment of unsteady viscous flow has proven to be applicable to a wide range of turbomachinery aeroelasticity problems. Ekici et al. provide a prime example with their investigation of flutter in a multistage compressor [4]. As realized in both references, the small disturbance Navier–Stokes equations are typically constructed to be hyperbolic in pseudotime, thus allowing the CFD-common temporal-marching techniques to be used in their solution. Generally, this pseudotime integration yields a converged solution without difficulty. In cases where the RANS supplied time-invariant mean flowfield exhibits phenomena associated with inherent physical unsteadiness (for example, areas of separation), solution divergence has sometimes been observed. Campobasso and Giles, however, show that the pseudotime integration can be stabilized by applying a generalized minimum residual (GMRES) approach to the derived linear equation system's solution at each pseudotime step [5]. The tradeoff lies in a more intricate algorithm as well as substantially higher memory requirements than experienced with conventional pseudotime-integration techniques. Incurring significantly less storage penalties than GMRES while being computationally competitive and equally robust, Campobasso and Giles subsequently suggested the recursive projection method (RPM) as an alternative means of stabilization [6].

Chassaing and Gerolymos provide a history of small disturbance Navier–Stokes methods, as well as their Euler predecessors, up to the year 2005 [7]. These are categorized by spatial dimension and discretization, the solution scheme, and (in case of the viscous methods) the employed turbulence model. Notably, it has been favored to fully account for the eddy viscosity's perturbation amplitude within the small disturbance Navier–Stokes equations, as

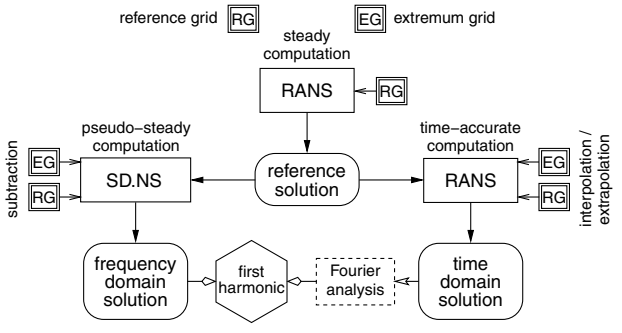

Fig. 1 Comparison between the small disturbance Navier–Stokes (SD. NS) and time-domain RANS computation processes.

Table 1 Computational advantages of the small disturbance approach over the dynamically fully nonlinear one

Aspect	Approach	
	Small disturbance	Dynamically fully nonlinear
Solution process	Single pseudosteady solution for the complex amplitude of the first harmonic	Time-accurate, typically requiring 300–400 successive pseudosteady solutions
Grid deformation	Unnecessary	Incremental
First-harmonic load	Obtained directly, in the scale of the disturbance	Fourier analysis [a]

[a]Considering the first-harmonic load to be an order of magnitude smaller than the zeroth-harmonic load, the former may be undesirably impacted by numerical errors incurred in its extraction as a small quantity from the entirety of the time-accurate periodic loading.

supplied by an accordant formulation of the Spalart–Allmaras (S/A) turbulence transport-equation and auxiliary functions [8]. This had also been the case in [4]. In the Chassaing and Gerolymos [7] recommendation, the destabilization of the derived linear equation system's solution would be most effectively countered by avoiding pseudotime integration altogether. This instance has been adopted by Petrie-Repar at the German Aerospace Center [9], directly applying a GMRES approach to the derived linear equation system. The robustness and performance of this unorthodox solution technique is demonstrated for two-dimensional compressor cascade test cases, yet still remains the topic of continuing investigations.

Lastly, it should be noted that the pioneers of the small disturbance Navier–Stokes method [3] have, meanwhile, further progressed toward an efficient dynamically fully nonlinear treatment of unsteady viscous turbomachinery flow by way of the harmonic-balance (HB) technique [10,11]. Executing a realized HB method with just a single harmonic, while letting the amplitude of the unsteady excitation go to nil, yields solutions equal to those obtained with a small disturbance Navier–Stokes method. The HB technique's advantage lies in a convenient formulation within the framework of an established steady-state RANS solver.

Whereas small disturbance Navier–Stokes methods have become the tool of choice in the turbomachinery industry to provide efficient and accurate aeroelastic predictions, their application to aircraft aeroelasticity is in its infancy.

Numerical Method

Over the past decade, research conducted at the former Aerodynamics Division of the Institute for Fluid Mechanics (FLM)[‡], Technical University of Munich, has ultimately resulted in the small disturbance Navier–Stokes method FLM-SD.NS. It had been realized as the viscous extension of the already well established small disturbance Euler method FLM-SDEu [12]. The two-dimensional incarnation of FLM-SD.NS for high-Reynolds-number flow was originally presented in [13], where a detailed derivation of the underlying governing equations and a synopsis of the general properties is given. Airfoil test cases demonstrated the approach's validity in the transonic regime. The introduction of the third spatial coordinate is straightforward and has been completed since then. In the development of FLM-SD.NS an effort had been made to retain numerical equivalence to the in-house RANS method FLM-NS [14], which is used, on the one hand, to supply the necessary time-invariant mean flowfield to FLM-SD.NS, while on the other hand, it is used to render a dynamically fully nonlinear solution of the particular unsteady case for comparative purposes.

Consequently, the cell-centered structured finite volume method FLM-SD.NS (multiblock capable) features small disturbance instances of Roe's convective flux-difference splitting [15] and of Chakravarthy's viscous flux evaluation [16]. Second-order spatial accuracy is given for smoothly stretched grids and regions of continuous flow, with the total variation diminishing condition yet satisfied at locations of discontinuity. A compliant derivation of the S/A turbulence model provides eddy viscosity closure, while a multigrid embedded lower-upper–symmetric-successive-overrelaxation (LU-SSOR) scheme adapted from Blazek [17] implicitly integrates the discretized governing equations in pseudotime. The generality of the spatial scheme is case-dependently restricted through the application of constraints at both the near- and far-field multiblock boundaries. Concerning the near field, small disturbance instances of the no-slip and adiabatic wall condition replace the slip condition inherent to FLM-SDEu. Equally imposed on the considered body's delimiting cell interfaces; these constraints are accounted for in the constitutive flux and turbulent source term vectors' evaluation at these localities. The algorithmic basis for both conditions' implementation is taken from the FLM-NS inherent instances. Concerning the far field, FLM-SDEu's characteristic-based treatment of perturbations at the extents of the regarded physical space is completely retained by FLM-SD.NS. This approach avoids an overdetermined in-/outflow constraint, giving the far-field boundary a degree of nonreflectivity [18]. As the already established FLM-methods (FLM-NS, FLM-SDEu, and the underlying dynamically fully nonlinear Euler method FLM-Eu [12]) all have been realized in the Fortran 90 programming language, it was continuously employed to implement the extension toward FLM-SD.NS.

Initial three-dimensional FLM-SD.NS computations were conducted for harmonic flap oscillations of both the NASA clipped delta wing (NCDW) [19] and a fighter-type delta wing (FTDW) in actual service [20] under high-Reynolds-number transonic flow conditions. Select results thereof were presented in [21], establishing the method's accuracy and efficiency. Reductions in computation time up to an order of magnitude in relation to FLM-NS were ascertained. Further substantiating the application readiness of FLM-SD.NS, computations for NCDW harmonic pitching oscillations under equivalent flow conditions are realized. The considered motion is governed by

$$\breve{\alpha}(k_{\mathrm{red}}\tau_s) = \breve{\bar{\alpha}} + \breve{\tilde{\alpha}}(k_{\mathrm{red}}\tau_s) \tag{1}$$

with

$$\breve{\tilde{\alpha}}(k_{\mathrm{red}}\tau_s) := \breve{\hat{\alpha}}\sin(k_{\mathrm{red}}\tau_s)$$

about the given pitch axis, with $\breve{\bar{\alpha}}$, $\breve{\hat{\alpha}}$, and $k_{\mathrm{red}} = 2\pi\breve{f}\breve{L}\sqrt{\breve{\rho}_\infty}/(Ma_\infty\sqrt{\gamma\breve{\rho}_\infty})$ set through the individual test case. The local unsteady load distribution normal to the wing's surface, embodied by $\bar{c}_p$, $\hat{c}_p$, as well as the resultant global loading, expressed by $\bar{c}_L$, $\hat{c}_L$ and $\bar{c}_M$, $\hat{c}_M$, are investigated. The latter are directly gained from the integration of the $\bar{c}_p$, $\hat{c}_p$, and correspondent skin-friction distributions over the wing's reference position surface. If desired, time-dependent c_p, c_L, and c_M evolutions can be gained by recomposite; that is,

$$\chi(k_{\mathrm{red}}\tau_s)|_{\mathrm{SD.NS}} := \bar{\chi} + \tilde{\chi}(k_{\mathrm{red}}\tau_s) \tag{2}$$

with

$$\tilde{\chi}(k_{\mathrm{red}}\tau_s) = \mathrm{Re}\hat{\chi}\sin(k_{\mathrm{red}}\tau_s) + \mathrm{Im}\hat{\chi}\cos(k_{\mathrm{red}}\tau_s)$$

The phase angle of $\hat{\chi}$ is given through

$$\breve{\varphi}_{\hat{\chi}} = \left[\frac{\pi}{2}\frac{\mathrm{Im}\hat{\chi}}{|\mathrm{Im}\hat{\chi}|}\left(1 - \frac{\mathrm{Re}\hat{\chi}}{|\mathrm{Re}\hat{\chi}|}\right) + \arctan\left(\frac{\mathrm{Im}\hat{\chi}}{\mathrm{Re}\hat{\chi}}\right)\right]180\ \mathrm{deg}/\pi$$

[‡]The FLM was reconstituted as the Institute of Aerodynamics in December 2004.

with $\breve{\varphi}_{\hat{\chi}} > 0$ indicating a $\tilde{\chi}$ that leads the excitation, and $\breve{\varphi}_{\hat{\chi}} < 0$ indicating a $\tilde{\chi}$ that lags the excitation, respectively, according to $\mathrm{Im}\hat{\chi} > 0$ and $\mathrm{Im}\hat{\chi} < 0$.

Determining the stability behavior of the corresponding free pitching oscillation, the systemic energy transfer by $\tilde{c}_M$ over the course of a single period is evaluated:

$$E = \int_{\tilde{\alpha}(0)}^{\tilde{\alpha}(2\pi)} \tilde{c}_M(\tilde{\alpha})\,\mathrm{d}\tilde{\alpha} \tag{3}$$

For $E > 0$, energy is periodically introduced into the system. Thus, $\tilde{c}_M$ has an amplifying effect, the free pitching oscillation then being classified as unstable. Complementary, for $E < 0$ energy is periodically withdrawn from the system. Thus, $\tilde{c}_M$ has a damping effect, the free pitching oscillation then being classified as stable. Actually resolving $\tilde{c}_M(\tilde{\alpha})$ and $\mathrm{d}\tilde{\alpha}$ of Eq. (3), it becomes apparent that E is merely a function of $\mathrm{Im}\hat{c}_M$ and $\hat{\alpha}$:

$$E = \int_0^{2\pi} [\mathrm{Re}\hat{c}_M\hat{\alpha}\sin(k_{\mathrm{red}}\tau_s)\cos(k_{\mathrm{red}}\tau_s) + \mathrm{Im}\hat{c}_M\hat{\alpha}\cos^2(k_{\mathrm{red}}\tau_s)]\,\mathrm{d}(k_{\mathrm{red}}\tau_s) = \pi\mathrm{Im}\hat{c}_M\hat{\alpha} \tag{4}$$

Hence, for $\hat{\alpha} > 0$ the free pitching oscillation can be classified as unstable if $\mathrm{Im}\hat{c}_M > 0$ or stable if $\mathrm{Im}\hat{c}_M < 0$, respectively, corresponding to a $\tilde{c}_M$ that leads or lags $\tilde{\alpha}$.

Prediction quality of FLM-SD.NS is primarily assessed by comparing its time-invariant mean and complex amplitude result (the load coefficients' zeroth and first harmonic) to the one yielding from the Fourier-analyzed FLM-NS time series. For a cycle of established periodicity, the load coefficients' zeroth harmonic is analytically gained as

$$\chi^0|_{\mathrm{NS}} := \frac{1}{2\pi}\int_0^{2\pi} \chi(k_{\mathrm{red}}\tau_s)|_{\mathrm{NS}}\,\mathrm{d}(k_{\mathrm{red}}\tau_s) \tag{5}$$

with

$$\mathrm{Re}\,\chi^j|_{\mathrm{NS}} := \frac{1}{\pi}\int_0^{2\pi} \chi(k_{\mathrm{red}}\tau_s)|_{\mathrm{NS}}\sin(jk_{\mathrm{red}}\tau_s)\,\mathrm{d}(k_{\mathrm{red}}\tau_s) \tag{6}$$

and

$$\mathrm{Im}\,\chi^j|_{\mathrm{NS}} := \frac{1}{\pi}\int_0^{2\pi} \chi(k_{\mathrm{red}}\tau_s)|_{\mathrm{NS}}\cos(jk_{\mathrm{red}}\tau_s)\,\mathrm{d}(k_{\mathrm{red}}\tau_s)$$

yielding the first harmonic for $j = 1$, as well as the higher harmonics for $j = 2, 3, \ldots, \infty$. Equations (5) and (6) are numerically evaluated with the trapezoidal rule, taking into account the number of employed physical time intervals. The discrete evolution of c_L and c_M itself arises from the integration of the c_p and skin-friction distributions over the deflected wing's surface after each converged physical time step.

For the purpose of comparison, the nomenclature of the FLM-SD.NS-computed load coefficients is brought into conformity with that common to the Fourier analysis:

$$\chi^0|_{\mathrm{SD.NS}} := \bar{\chi}; \qquad \chi^1|_{\mathrm{SD.NS}} := \hat{\chi} \tag{7}$$

Inviscid results computed with FLM-SDEu and FLM-Eu are additionally drawn upon to emphasize the impact of viscosity. Both FLM-NS and FLM-Eu render the unsteady aerodynamic loading with second-order accuracy in time. Experimental surface pressure data are also taken into account. The globally used Cartesian coordinate system is set to originate from the wing's root leading edge (LE) at reference position, with the x (chordwise) direction running positively toward the trailing edge (TE) and the y (spanwise) direction running positively toward the starboard tip. The imposed motion is strictly longitudinal, that is, occurring about an axis parallel to the spanwise direction. Consequently, a semispan numerical treatment of the NCDW suffices, the starboard half being considered here.

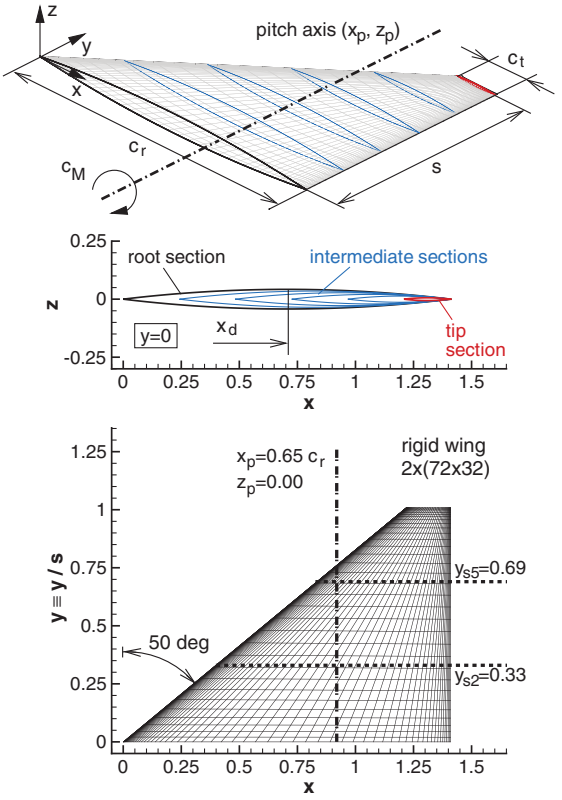

Fig. 2 Composited spatial cross-sectional and planform view (surface grid with superimposed pitch axis and investigated span stations) of the rendered NCDW.

NASA Clipped Delta Wing

Derived from the wing of a tentative supersonic transport, the NCDW is characterized by a 50 deg swept LE, an unswept TE, and a symmetrical circular arc section of constant 6% relative thickness across the span ($x_d/c = 0.5$, sharp LE/TE), sans twist (Fig. 2). In its semispan instance ($\breve{L} := \breve{s} = 1.145$ m), the planform is trapezoidal, with $s := \breve{s}/\breve{L} = 1.0$ and $c_r := \breve{c}_r/\breve{L} = 1.410$ supplementing the sweep angles in the definition. The secondary geometric properties result to $\lambda = 0.142$,

$$A := \breve{A}/\breve{L}^2 = 0.805; \qquad \left(A = \int_0^s c\,dy\right)$$

$\mathrm{AR} = 1.242$, $c_{\mathrm{av}} := \breve{c}_{\mathrm{av}}/\breve{L} = 0.805$, and

$$c_\mu := \breve{c}_\mu/\breve{L} = 0.956; \qquad \left(c_\mu = \int_0^s c^2 dy/A\right)$$

while the pitch axis resides at $x_p/c_r = 0.65$ and $z_p = 0.00$. Surface pressure distributions were evaluated at six distinct span stations, of which all but the innermost correspond to those instrumented on the test model. Data for merely one inner- and one outer-span station, respectively, $y_{s2} := y/s = 0.33$ and $y_{s5} = 0.69$, will be discussed here.

The upper and lower surface of the NCDW's numerical embodiment are each discretized with 72 cells (hyperbolically distributed) in chordwise and 32 cells (Poisson-distributed) in spanwise direction, for a total of 2304 cells per surface. It is embedded (at reference position) in an elliptically smoothed two-block C-H-topology structured volume grid by way of a boundary-fitted ($\xi\eta\zeta$) coordinate system (Fig. 3). The far-field distances are set to $11 \times s$ in positive chordwise direction from the root LE, to $11 \times s$ in both positive and negative vertical (z) direction from the root TE, as well as to $5 \times s$ in spanwise direction respective the wing's lateral (xz) plane of symmetry. Each block discretizes one half of the numerically treated physical domain as divided by the wing's vertical

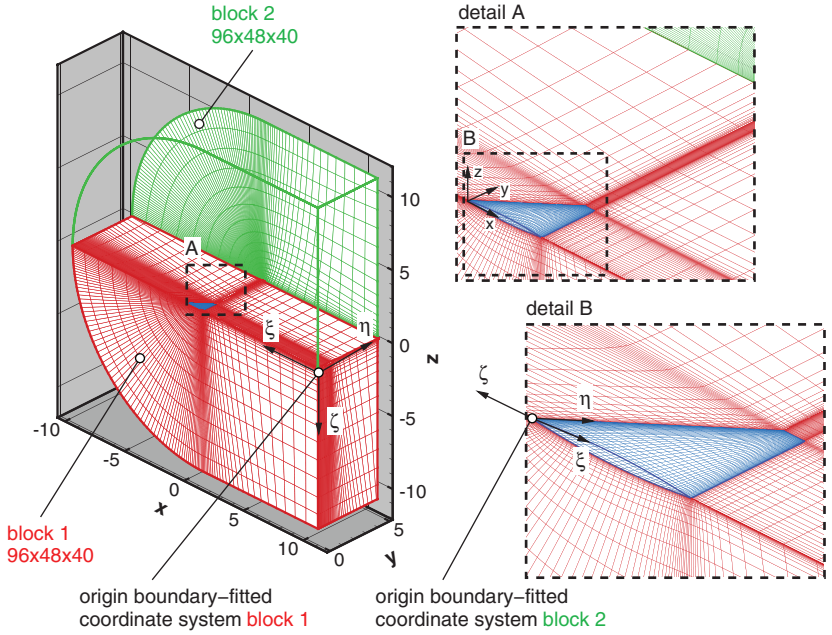

Fig. 3 Rendered NCDW embedded in an elliptically smoothed two-block C-H-topology structured volume grid.

(xy) plane of symmetry. Thus, the individual block is associated with strictly one of the wing's surfaces, either the upper or lower. It discretizes the delimited volume with 96 cells in positive chordwise, 48 cells in spanwise, and 40 cells in wing surface normal direction, translating into 184,320 cells per block or 368,640 cells for the entire grid. Cells in the wing-surface normal direction are hyperbolically distributed, the distance of the first offbody grid plane being set to $1 \times 10^{-5} \times s$. For the considered high-Reynolds-number transonic flow this renders a $d^+ < 5$, as required by the S/A turbulence model. The chosen two block topology allows orthogonality of grid lines emanating from the upper and lower surface in proximity to the LE. Regeneration of the volume grid for the $\check{\bar{\alpha}}$-rotated surface grid and subsequent smoothing ultimately yields the desired extremum grid. Hence, its global properties are equivalent to those of the reference grid. Further details on grid construction and smoothing are given in [22].

From the multitude of available dynamic test cases, results for a weak shock case (90D5), the medium-strength shock/leading-edge vortex (LEV) case (90D29), and a strong shock case (94D5) are presented. On the basis of 94D5, both a case at lower (94D4) and higher frequency (94D6) are computed as well, however, they have no experimental equivalent. Table 2 provides the computation parameters for each case. All cases have $Re_\infty = 10.0 \times 10^6$, $\gamma = 1.132$, $Pr = 0.775$ (heavy gas), and $Pr_t = 0.90$ in common. FLM-SD.NS computations employ a three-level V-symmetric multigrid cycle for acceleration. Per multigrid-cycle dual-pseudotime steps on the finest and coarsest grid levels, in combination with a single-pseudotime step on the intermediary level (2/1/2), are conducted. A converged solution of the governing equations is assumed when the L_2-norm amplitude density residual, as normalized with its value after the first multigrid cycle, has dropped below 5.5×10^{-4} (5.0×10^{-4} for 90D29), terminating the computation. Instability of the solution process was initially experienced for cases 94D4-6, where a confined region of postshock separation occurs toward the wing tip in the time-invariant mean flowfield. After a number of multigrid cycles the $\hat{\tilde{\mu}}$ residual begins to diverge, eventually leading to its exponential growth. As the incurred distortion of the amplitude flowfield increases in significance, the amplitude density residual follows suit. This is reminiscent of the behavior encountered by Campobasso and Giles [5,6] with their conventional pseudotime-integration scheme. Specifically, the instability can be traced to the evaluation of the reference-metric-homogenous amplitude S/A source term within the region of separated flow. The localized limitation of $\hat{\tilde{\mu}}$; that is,

$$\sigma|_{\text{lim}} := \frac{\sigma}{|\sigma|}\min(|\sigma|,\ \bar{\tilde{\mu}}) \tag{8}$$

with

$$\sigma \in \{\text{Re}\hat{\tilde{\mu}},\ \text{Im}\hat{\tilde{\mu}}\}$$

in each cell, allowed for stabilization, without having to resort to the GMRES approach or RPM. Implementationwise, Eq. (8) becomes part of the LU-SSOR algorithm, applied to the amplitude state vector's update within the backward sweep. In effect, the $\hat{\tilde{\mu}}$ residual decreases and subsequently progresses toward an asymptote, allowing the amplitude density residual to converge to the desired level of accuracy (Fig. 4). As will be shown, the limiter's activation does not lead to any noteworthy degradation of the load prediction. For cases with substantial regions of separation contained in the time-invariant mean flowfield the limiter's impact remains to be assessed.

For the comparative FLM-NS computations three oscillation cycles suffice to achieve load coefficient periodicity, each discretized with 100 physical time intervals. Incremental grid deformation is carried out through time-law-accordant interpolation and extrapolation between the extremum and reference grid. Multigrid parameters and abort criterion are set equal to those of the

Table 2 Computation parameters of the NCDW cases

Case	Ma_∞	$\check{\bar{\alpha}}$, deg	$\check{\hat{\alpha}}$, deg	k_{red}	$\check{f}$, Hz	$\check{p}_\infty$, kPa	$\check{\rho}_\infty$, kg/m^3	$\check{T}_\infty$, K
90D5	0.90	0.00	0.50	0.237	8.0	20.7	0.326	298.4
90D29	0.90	3.97	0.50	0.240	8.0	20.5	0.329	298.9
94D4	0.94	0.00	0.50	0.115	4.0	19.3	0.313	295.5
94D5	0.94	0.00	0.50	0.230	8.0	19.3	0.313	295.5
94D6	0.94	0.00	0.50	0.460	16.0	19.3	0.313	295.5

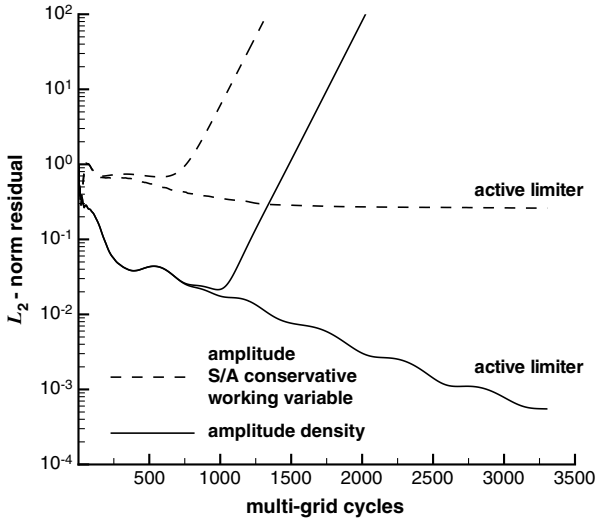

Fig. 4 Comparison of the FLM-SD.NS residual history, with and without active limiter, for the NCDW case 94D5 ($Ma_\infty = 0.94$, $Re_\infty = 10.0 \times 10^6$, $\breve{\bar{\alpha}} = 0.0$ deg, $\hat{\breve{\alpha}} = 0.5$ deg, $k_{\text{red}} = 0.230$, $x_p/c_r = 0.65$).

FLM-SD.NS computations. The FLM-SD.NS/FLM-NS computation of 90D5, and 90D29, were conducted on a single 1.3 GHz Intel Itanium 2 processor of the Leibniz–Rechenzentrum Linux cluster, with 94D4-6 subsequently realized on a 1.6 GHz successor model. The FLM-method machine code was generated with the Intel Fortran Compiler for Linux.

Generally, the supplemental FLM-SDEu/FLM-Eu computations employ the same reference and extremum grid as the FLM-SD.NS/FLM-NS ones in order to retain spatial comparability. For 90D29, however, the high resolution of the wing's near-field destabilized the inviscid solution process, necessitating the consideration of more Euler-typical grids. These are internally generated from the Navier–Stokes grids through elimination of every other cell edge, rendering coarser grids of 46,080 cells, with 576 cells per surface. This constitutes a substantial reduction, respectively, by 88% and 75%. Nevertheless, the wing surface and near-field remain sufficiently resolved, with the distance of the first offbody grid plane only increasing to $3 \times 10^{-5} \times s$. It should be noted, that the experimental surface pressure data of the dynamic test cases are limited to the first harmonic. Thus, for zeroth-harmonic comparison the experimental surface pressure data of the underlying static test case are drawn upon. Each represents the NCDW investigated under congruous ambient conditions yet fixed at its $\breve{\bar{\alpha}}$. For 90D5, 90D29, and 94D4-6, these are 90S1, 90S38, and 94S1 [19], respectively. In the following, the load coefficients' real and imaginary parts are normalized with $\breve{\bar{\alpha}}\pi/180$ deg.

Results and Discussion

Weak Shock Case

For $Ma_\infty = 0.90$, $Re_\infty = 10.0 \times 10^6$, and $\breve{\bar{\alpha}} = 0.0$ deg, the FLM-NS supplied time-invariant mean flowfield exhibits a localized, equally developed, supersonic region in proximity to the upper and lower wing surface. It extends, respectively, from the root to the tip, terminating with a weak shock significantly upstream of the TE (Fig. 5). FLM-SD.NS-computed surface pressure distributions for 90D5 are composited with their FLM-NS and FLM-SDEu/FLM-Eu, and with their experimental counterparts in Fig. 6. The FLM-SD.NS result is described in the following. Upper- and lower-surface c_p^0, of course, exhibit symmetry. From root to tip the onset of supersonic flow moves substantially closer to the LE. In contrast, the termination (indicative of the shock base) varies far less in its chordwise locality, with the weak shock merely imposing a shallow slope onto the c_p^0 progression. Obviously, symmetry of the upper- and lower-surface c_p^0 yields numerically nil c_L^0 and c_M^0 values.

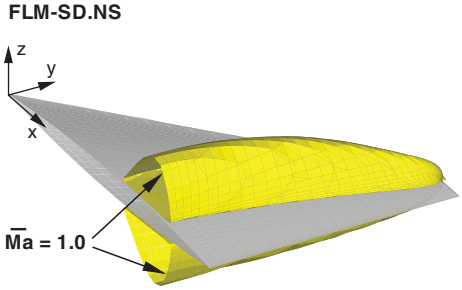

Fig. 5 Sonic isosurface of the time-invariant mean flowfield employed by FLM-SD.NS in the NCDW case 90D5 ($Ma_\infty = 0.90$, $Re_\infty = 10.0 \times 10^6$, $\breve{\bar{\alpha}} = 0.0$ deg, $\hat{\breve{\alpha}} = 0.5$ deg, $k_{\text{red}} = 0.237$, $x_p/c_r = 0.65$).

Complementary to c_p^0, upper- and lower-surface $\mathrm{Re}c_p^1$, as well as $\mathrm{Im}c_p^1$, exhibit antisymmetry. Merely considering the upper-surface distribution, the sharp LE renders an initial primary peak for both $\mathrm{Re}c_p^1$ and $\mathrm{Im}c_p^1$, respectively, being of negative and positive value. Immediately downstream, $\mathrm{Re}c_p^1$ acutely increases before leveling off. In case of the inner-span station, a mild secondary $\mathrm{Re}c_p^1$ peak emerges at the location of minimum c_p^0. It leads into a strong increase across the shock region, culminating in a reversal of sign for $\mathrm{Re}c_p^1$ at the location of the terminating $c_{p,\text{crit}}^0$. Subsequently, the $\mathrm{Re}c_p^1$ progression follows through to postshock positivity. It reaches a local maximum before decreasing toward the TE, where equalization with the lower-surface $\mathrm{Re}c_p^1$ occurs at nil value. For the outer-span station, the further $\mathrm{Re}c_p^1$ progression toward the TE qualitatively corresponds to that of the inner one, however, lacks the mild secondary peak. Evidently, $\Delta\mathrm{Re}c_p^1$ forward of the zero-crossing supplies the bulk of $\mathrm{Re}c_L^1$. Its positive contribution is only marginally compensated by the aft difference's negative one. Evaluation of $\mathrm{Re}c_M^1$ proves to be more difficult as leverage respective the pitch axis must also be taken into account. The positive $\Delta\mathrm{Re}c_p^1$ forward of the zero-crossing can contribute in equal magnitude both positively (pitch up) and negatively (pitch down) to $\mathrm{Re}c_M^1$. The negative $\Delta\mathrm{Re}c_p^1$ aft of the zero-crossing, on the other hand, makes an unambiguous positive (pitch up) contribution through its leverage. Integrating over the entire wing, both a positive $\mathrm{Re}c_L^1$ and $\mathrm{Re}c_M^1$ are ascertained.

For the inner-span station, $\mathrm{Im}c_p^1$ acutely decreases from its LE peak, leading into a nearly linear progression that ends slightly upstream of the shock region. Before ending, a reversal of sign is experienced. This places the subsequent shock and postshock progression into negative territory. A secondary peak is exhibited at the location of the terminating $c_{p,\text{crit}}^0$. $\mathrm{Im}c_p^1$ increases from there toward the TE, where equalization with its lower-surface counterpart takes place. The $\mathrm{Im}c_p^1$ progression of the outer-span station qualitatively corresponds to that of the inner one. Forward of the zero-crossing, $\Delta\mathrm{Im}c_p^1$ contributes negatively to $\mathrm{Im}c_L^1$, while its aft counterpart does so positively. Both are approximately equal in magnitude, largely canceling each other out in the sectional $\mathrm{Im}c_L^1$. For the inner-span station, the pitch axis intersects closely to the exhibited zero-crossing. Thus, both forward and aft $\Delta\mathrm{Im}c_p^1$ can be said to render a negative (pitch down) contribution to $\mathrm{Im}c_M^1$. As the intersection of the pitch axis moves closer to the LE for the outer-span station, merely the aft $\Delta\mathrm{Im}c_p^1$ can be identified to have an unambiguously negative (pitch down) contribution to $\mathrm{Im}c_M^1$. Integrating over the entire wing, both a negative $\mathrm{Im}c_L^1$ and $\mathrm{Im}c_M^1$ (pitch down) are ascertained, however, with $\mathrm{Im}c_L^1$ being an order of magnitude smaller in absolute value than $\mathrm{Re}c_L^1$.

For the investigated span stations, FLM-SD.NS-computed c_p^0, $\mathrm{Re}c_p^1$, and $\mathrm{Im}c_p^1$ agree excellently with those obtained from FLM-NS. Mild discrepancies are observed in the shock and postshock region. Evidently, the small disturbance premise holds up under the dynamic nonlinearity of the weak shock. The conformity between FLM-SD.NS and FLM-NS can be seen equal to that between FLM-SDEu and FLM-Eu. Viscous and inviscid c_p^0 differ only marginally in the shock region, with greater variation becoming noticeable for their $\mathrm{Re}c_p^1$ and $\mathrm{Im}c_p^1$ counterparts. In particular, the inviscid methods predict a mild secondary $\mathrm{Re}c_p^1$ peak that persists from the inner- to the outer-span station. Disregarding outliers, experimental surface pressure is reproduced well. Surprisingly, the data points rendering

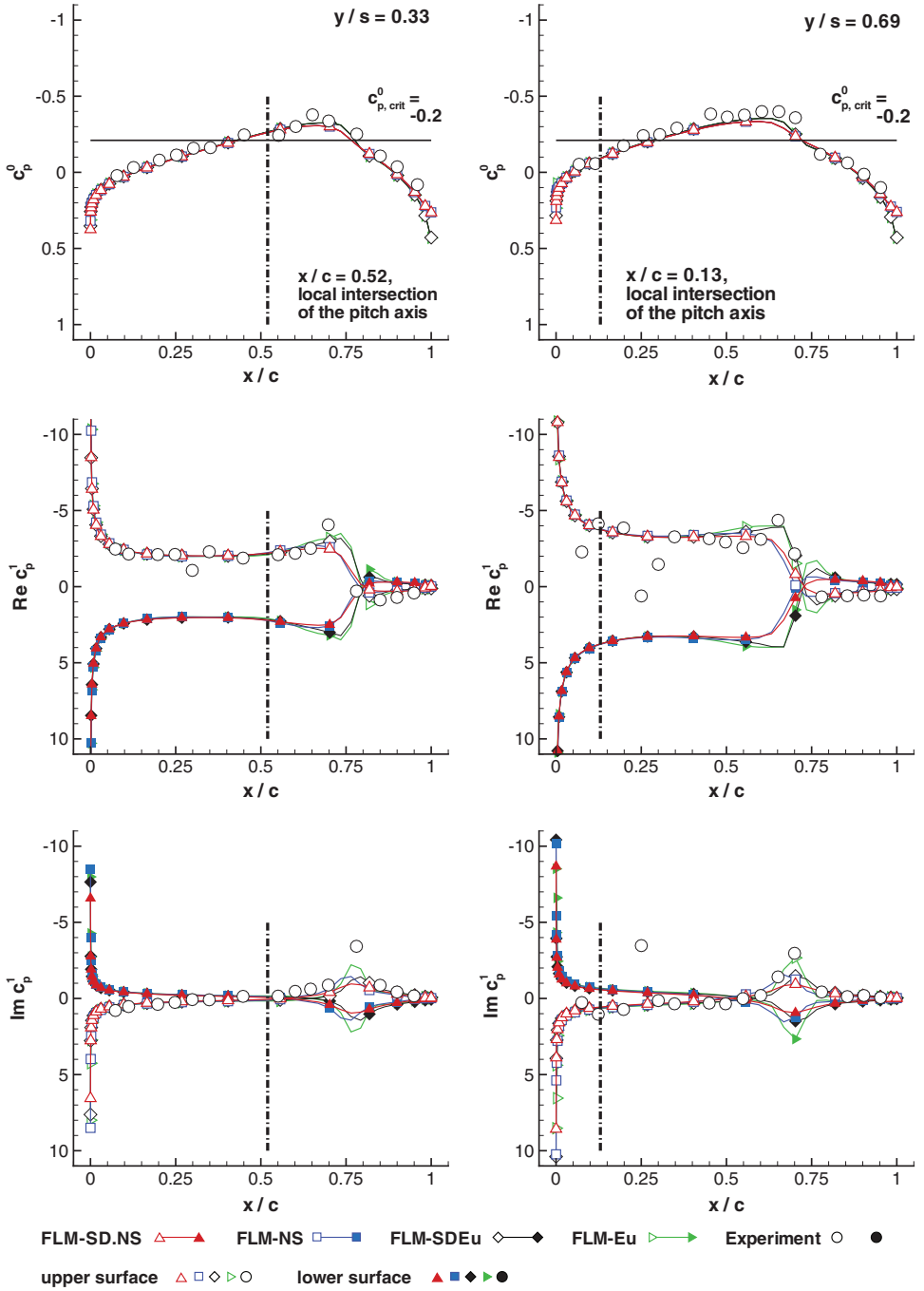

Fig. 6 Comparison of the zeroth- and first-harmonic pressure coefficient distributions (c_p^0 and c_p^1) for the NCDW case 90D5 ($Ma_\infty = 0.90$, $Re_\infty = 10.0 \times 10^6$, $\breve{\alpha} = 0.0$ deg, $\hat{\breve{\alpha}} = 0.5$ deg, $k_{\text{red}} = 0.237$, $x_p/c_r = 0.65$).

the secondary $\text{Re}c_p^1$ and $\text{Im}c_p^1$ peak are best met by the FLM-Eu computation.

Focusing on the computed global load coefficients (Table 3), $\text{Re}c_L^1$ gained from FLM-SD.NS agrees excellently to its FLM-NS counterpart. $\text{Im}c_L^1$, on the other hand, is predicted 10% higher in absolute value. This deviation, however, becomes acceptable when taking the 2 orders of magnitude into account that separate $\text{Re}c_L^1$ from $\text{Im}c_L^1$. Both FLM-SDEu- and FLM-Eu-computed $\text{Re}c_L^1$ are 5% higher than their viscous counterparts, attributable to the differing prediction of $\text{Re}c_p^1$ in the shock region. Their mutual deviation is similarly negligible. With FLM-SDEu $\text{Im}c_L^1$ is gained equal to its FLM-SD.NS-predicted instance, disregarded viscosity apparently

Table 3 Comparison of the global load coefficients for NCDW case 90D5 ($Ma_\infty = 0.90$, $Re_\infty = 10.0 \times 10^6$, $\breve{\alpha} = 0.0$ deg, $\hat{\breve{\alpha}} = 0.5$ deg, $k_{\text{red}} = 0.237$, $x_p/c_r = 0.65$)

Method	c_L^0	$\text{Re}c_L^1$	$\text{Im}c_L^1$	$\lvert c_L^1\rvert$	$\breve{\varphi}_{c_L^1}$, deg	c_M^0	$\text{Re}c_M^1$	$\text{Im}c_M^1$	$\lvert c_M^1\rvert$	$\breve{\varphi}_{c_M^1}$, deg
FLM-SD.NS	0.000	3.748	−0.013	3.748	−0.20	0.000	0.322	−0.178	0.368	−28.87
FLM-NS	0.000	3.762	−0.012	3.762	−0.18	0.000	0.333	−0.196	0.387	−30.51
FLM-SDEu	0.000	3.956	−0.013	3.956	−0.19	0.000	0.271	−0.196	0.335	−35.84
FLM-Eu	0.000	3.962	0.007	3.962	0.11	0.000	0.285	−0.222	0.361	−37.88

having no impact. Surprisingly, $\mathrm{Im}c_L^1$ obtained from FLM-Eu exhibits a positive sign, while remaining within the same order of magnitude as its FLM-SDEu counterpart.

FLM-SD.NS-computed $\mathrm{Re}c_M^1$ and $\mathrm{Im}c_M^1$ are, respectively, 3% and 9% lower in absolute value than their FLM-NS counterparts. Evidently, the deviation exhibited in $\mathrm{Im}c_L^1$ has followed through to $\mathrm{Im}c_M^1$. $\mathrm{Re}c_M^1$ and $\mathrm{Im}c_M^1$ are now in the same order of magnitude. The time-dependent c_M clearly lags the excitation, which in case of a free pitching oscillation would have a damping effect. FLM-SDEu- and FLM-Eu-computed $\mathrm{Re}c_M^1$ are, respectively, 16% and 14% lower than their viscous counterparts. The particular $\mathrm{Im}c_M^1$ instances, on the other hand, are 10% and 13% higher in absolute value. Disregarded viscosity has a more noticeable impact on c_M^1 than on c_L^1, with the inviscid $\mathrm{Im}c_M^1$ indicating greater dynamic stability. Deviation between FLM-SDEu- and FLM-Eu-computed instances is similar to the one shown by the corresponding viscous methods.

Overall, FLM-SD.NS renders the unsteady loading of the weak shock case in very good agreement to FLM-NS. For either method the viscous consideration yields a c_M^1-prediction that improves on the respective inviscid approach.

Medium-Strength Shock/Leading-Edge Vortex Case

For $Ma_\infty = 0.90$, $Re_\infty = 10.0 \times 10^6$, and $\breve{\alpha} = 3.97$ deg, the FLM-NS supplied time-invariant mean flowfield exhibits an expanded supersonic region in proximity to the upper wing surface. It extends from the root to the tip, terminating with a medium-strength shock significantly upstream of the TE (Fig. 7). At the root, the sharp LE additionally initiates a vortex that convects toward the tip (Fig. 8). The LE itself approximately renders the line of separation, while the line of reattachment is observed at a sweep angle of 56 deg. Designated the LEV, it induces a localized suction plateau on the upper surface which increases in both intensity and expansion over the course of the progression, $\bar{c}_p$ reaching its minimum value at the LE and $y/s \approx 0.95$. Toward the tip, the LEV has intersected the shock ($y/s \approx 0.80$), the interaction between the two rendering quite the intricate flow topology. FLM-SD.NS-computed surface pressure distributions for 90D29 are composited with their FLM-NS, FLM-SDEu/FLM-Eu, and with their experimental counterparts in Fig. 9. The FLM-SD.NS result is subsequently described. Considering the inner-span station first, the sharp LE renders an initial suction peak for the upper-surface c_p^0 progression. It acutely increases immediately downstream, a tightly constrained suction plateau induced by the LEV. As rotational velocity abruptly subsides beyond the line of reattachment ($x/c = 0.10$), c_p^0 again increases steeply, eventually leading into a local maximum. The further acceleration from subsonic to supersonic speeds produces a linearly decreasing c_p^0 that culminates in a local minimum before the discontinuous recompression, the medium-strength shock. As supersonic flow terminates, the remaining recompression toward the TE is strictly continuous. In contrast, the convex lower-surface c_p^0 progression never falls below $c_{p,\mathrm{crit}}^0$, indicating subsonic flow from LE to TE. Notably, the continuous recompression toward the TE occurs with a c_p^0 of lesser value than observed for the upper-surface, equalization eventually taking place at the TE. Apparently, the positive contribution to c_L^0 made by Δc_p^0 forward of both progressions' intersection is only marginally compensated by the negative one aft of it. In accordance, Δc_p^0 leveraged respective the pitch axis unambiguously yields a positive (pitch up) net contribution to c_M^0.

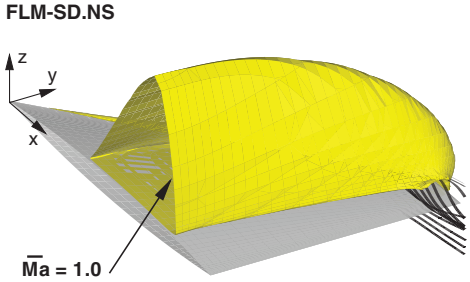

Fig. 7 Sonic isosurface of the time-invariant mean flowfield employed by FLM-SD.NS in the NCDW case 90D29 ($Ma_\infty = 0.90$, $Re_\infty = 10.0 \times 10^6$, $\breve{\alpha} = 3.97$ deg, $\breve{\alpha} = 0.5$ deg, $k_{\mathrm{red}} = 0.240$, $x_p/c_r = 0.65$).

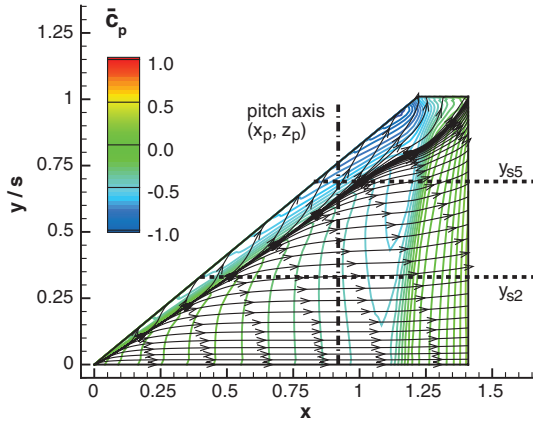

Fig. 8 Near-surface streamlines and surface isobars of the time-invariant mean flowfield employed by FLM-SD.NS in the NCDW case 90D29 ($Ma_\infty = 0.90$, $Re_\infty = 10.0 \times 10^6$, $\breve{\alpha} = 3.97$ deg, $\breve{\alpha} = 0.5$ deg, $k_{\mathrm{red}} = 0.240$, $x_p/c_r = 0.65$).

The c_p^0 progressions of the outer-span station are qualitatively similar to their inner counterparts. In regard to the upper surface, the suction plateau is now observed to range farther downstream, as the extent of the LEV has grown. Shortly beyond the line of reattachment ($x/c = 0.27$) the flow has already become supersonic. Accelerating further, c_p^0 again decreases linearly downstream, however, now over a far shorter distance. The local minimum preceding the discontinuous recompression is exhibited farther upstream relative to the local chord length than its inner-span-station counterpart. The latter can also be observed for the $c_{p,\mathrm{crit}}^0$-indicated shock base. For the lower surface, c_p^0 still indicates entirely subsonic flow, with the convex progression now intersecting its upper-surface counterpart farther upstream relative to the chord length. Whereas Δc_p^0 again yields a substantial positive contribution to c_L^0, its leverage with respect to the pitch axis now renders a differingly negative (pitch down) contribution to c_M^0. Integrating over the entire wing though, both a positive c_L^0 and c_M^0 (pitch up) are ascertained.

Common to the inner- and outer-span station, the upper-surface $\mathrm{Re}c_p^1$ progression is characterized by a forward and aft negative peak, respectively, ascribed to the implied motion of the LEV and shock. They are interconnected by a region of nearly constant $\mathrm{Re}c_p^1$. Postshock, $\mathrm{Re}c_p^1$ increases abruptly, leading into a positive value progression which ultimately decreases toward the TE, a reversal of sign occurring again shortly before reaching it. Comparing the $\mathrm{Re}c_p^1$ progression of the inner- and outer-span station, the LEV-induced peak has moved farther downstream relative to the local chord length for the latter. It exhibits a decrease in value and a greatly widened base. Vice versa, the shock-induced peak is now situated farther upstream while its value has increased. The base of the shock-induced peak, however, widens only slightly. As a consequence of both the LEV- and shock-induced occurrences, the interconnecting region of nearly constant $\mathrm{Re}c_p^1$ has reduced to a small fraction of the chord length. The inner- and outer-span-station instances of the lower-surface $\mathrm{Re}c_p^1$ progression are again similar. They increase acutely from the LE toward a nearly constant value that ranges downstream. Subsequently decreasing, the progressions intersect their upper-surface counterparts, reverse sign, and finally equalize at the TE. In either case, the positive $\mathrm{Re}c_L^1$ contribution made by $\Delta\mathrm{Re}c_p^1$ forward of the intersection is only marginally compensated by the negative one aft of it. For the inner-span station, $\Delta\mathrm{Re}c_p^1$ leveraged respective the pitch axis will unambiguously yield a positive (pitch up) net contribution to $\mathrm{Re}c_M^1$. For the outer-span station, on the other hand, it will result in a differingly negative (pitch down) net

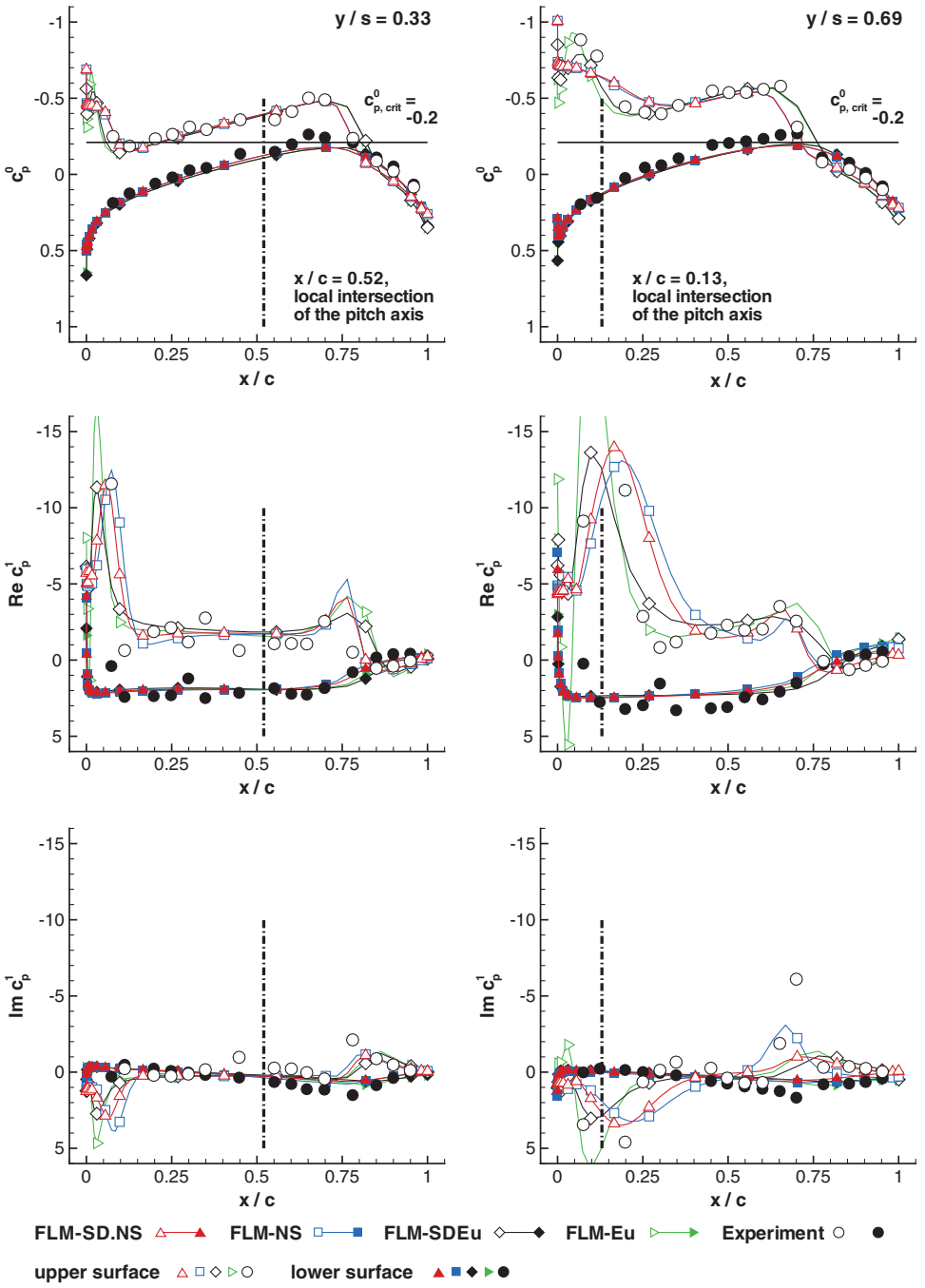

Fig. 9 Comparison of the zeroth- and first-harmonic pressure coefficient distributions (c_p^0 and c_p^1) for the NCDW case 90D29 ($Ma_\infty = 0.90$, $Re_\infty = 10.0 \times 10^6$, $\breve{\alpha} = 3.97$ deg, $\hat{\breve{\alpha}} = 0.5$ deg, $k_{\text{red}} = 0.240$, $x_p/c_r = 0.65$).

contribution. Integrating over the entire wing though, both a positive $\text{Re}c_L^1$ and $\text{Re}c_M^1$ (pitch up) are ascertained.

Naturally, the implied motion of the LEV and shock also leaves its trace on the upper-surface $\text{Im}c_p^1$ progression. For both the inner- and outer-span station a forward positive and aft negative peak have developed, however, being of substantially lower absolute value than their upper-surface $\text{Re}c_p^1$ counterparts. They are interconnected by a region of nearly constant $\text{Im}c_p^1$, all in all observed as a progression close to nil value. Comparing the $\text{Im}c_p^1$ progression of the inner- and outer-span station, the LEV-induced peak has again moved downstream relative to the local chord length for the latter, while being higher in $\text{Im}c_p^1$ value. Vice versa, the shock-induced peak is now situated farther upstream relative to the local chord length, with the $\text{Im}c_p^1$ value being nearly unchanged. The base of both the LEV- and shock-induced peak have widened to the point where the decreasing progression of the former directly leads into that of the latter. Notably, the differing sign witnessed in the peak $\text{Im}c_p^1$ values of either span station indicates a reversal in phase, from leading to lagging, between these two instances. For both the inner- and outer-span station, the lower-surface $\text{Im}c_p^1$ progression can be observed to be close to nil value, allowing the corresponding time-dependent c_p to be considered essentially in phase. $\Delta\text{Im}c_p^1$ resulting from the LEV-induced peak contributes negatively to the sectional $\text{Im}c_L^1$, whereas the one resulting from the shock-induced peak does so positively. With respect to each span station, however, the two largely cancel each other out. Considering leverage to the pitch axis, the forward and aft $\Delta\text{Im}c_p^1$ both render an unambiguous negative (pitch down) contribution to $\text{Im}c_M^1$ for the inner-span station. In case of the outer-span station, the negative $\Delta\text{Im}c_p^1$ resulting from the LEV-induced peak now contributes both negatively (pitch down) and positively (pitch up) to $\text{Im}c_M^1$. The positive $\Delta\text{Im}c_p^1$ resulting from the shock-induced peak, however, still contributes negatively (pitch down) to

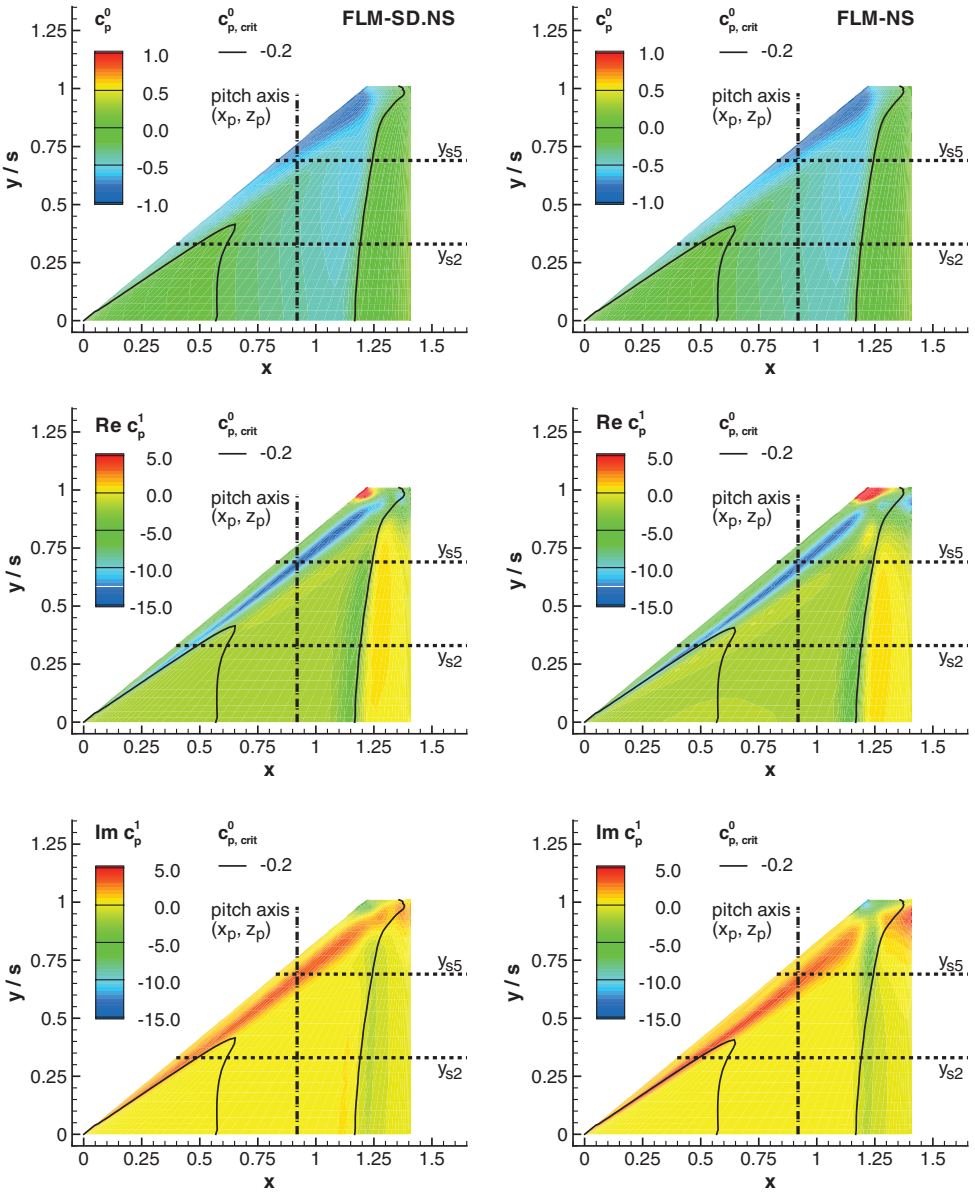

Fig. 10 FLM-SD.NS- and FLM-NS-computed planform upper-surface zeroth- and first-harmonic pressure coefficient distributions (c_p^0 and c_p^1) for the NCDW case 90D29 ($Ma_\infty = 0.90$, $Re_\infty = 10.0 \times 10^6$, $\breve{\alpha} = 3.97$ deg, $\hat{\breve{\alpha}} = 0.5$ deg, $k_{\text{red}} = 0.240$, $x_p/c_r = 0.65$).

$\text{Im}c_M^1$. Integrating over the entire wing, both a negative $\text{Im}c_L^1$ and $\text{Im}c_M^1$ (pitch down) are ascertained, however, with $\text{Im}c_L^1$ being an order of magnitude smaller in absolute value than $\text{Re}c_L^1$. From the outer-span station toward the tip, the occurrences in the c_p^0, $\text{Re}c_p^1$, and $\text{Im}c_p^1$ progressions distinctly associated with the LEV and the shock become more diffuse. They eventually merge into a single instance beyond the span station of intersection (Fig. 10).

For the investigated span stations, FLM-SD.NS-computed upper- and lower-surface c_p^0 agrees excellently with those obtained from FLM-NS (Fig. 9). Respective $\text{Re}c_p^1$, mild discrepancies are observed for the predicted LEV- and shock-induced peaks of the inner-span station, however, growing larger for the outer one. Postshock deviations are also witnessed here for both the upper- and lower-surface $\text{Re}c_p^1$ progression toward the TE. Otherwise, the lower-surface $\text{Re}c_p^1$ agrees excellently, as linear flow physics are dominant. With the exception of a localized region from $y/s = 0.80$ to the tip, lower-surface flow remains subsonic over the entire course of an oscillation. Naturally, the lower-surface $\text{Im}c_p^1$ agrees excellently as well. In regard to upper-surface $\text{Im}c_p^1$, mild discrepancies are observed for the predicted LEV- and shock-induced peaks of the inner-span station, which yet again increase for the outer one. Here the deviation between the FLM-SD.NS and FLM-NS-predicted shock-induced peak becomes very substantial, indicating that the premise of the dynamically linear approach may no longer be valid farther outboard. Investigating this matter, the FLM-SD.NS-computed planform upper-surface c_p^0, c_p^1 distributions are compared with the planform upper-surface c_p^0, c_p^1, as well as planform upper-surface second and third harmonic pressure coefficient distributions (c_p^2, c_p^3) gained from FLM-NS (Fig. 10 and 11). Apparently, even for a small amplitude of $\hat{\breve{\alpha}} = 0.5$ deg, the imposed motion on the LEV and its dynamic interaction with the shock are sufficient to induce higher-order harmonics within the time-dependent evolution of the upper-surface c_p. It can be observed that both c_p^2 and c_p^3 locally exceed the specified 10% c_p^1 range, in parts significantly. For regions where $c_p^0 \gg c_p^1 \gg c_p^2 \gg c_p^3$ no longer holds true, however, the small disturbance method cannot render an accurate c_p^1 prediction. As higher-order harmonics become dominant in the flowfield they exert influence on those of lower order (nonlinear interaction). Consequently, the time-invariant mean flowfield employed by the dynamically linear approach will depart from the actual zeroth-harmonic one. The complex amplitude flowfield computed by

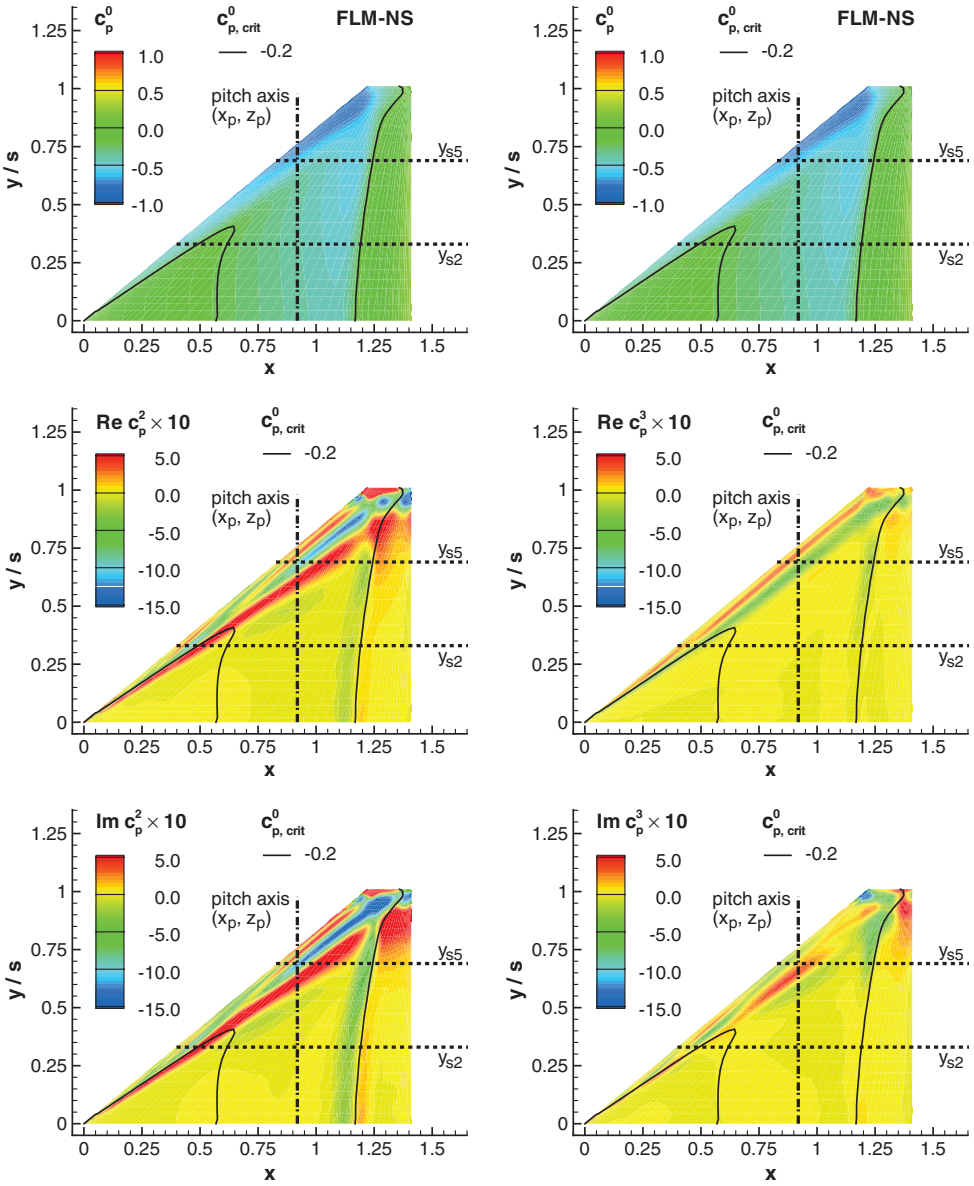

Fig. 11 FLM-NS-computed planform upper-surface zeroth-, second-, and third-harmonic pressure coefficient distributions (c_p^0, c_p^2, and c_p^3) for the NCDW case 90D29 ($Ma_\infty = 0.90$, $Re_\infty = 10.0 \times 10^6$, $\breve{\bar{\alpha}} = 3.97$ deg, $\hat{\bar{\alpha}} = 0.5$ deg, $k_{\text{red}} = 0.240$, $x_p/c_r = 0.65$).

FLM-SD.NS can then only deviate from the actual first-harmonic one as well.

Revisiting Fig. 9, the conformity between FLM-SD.NS and FLM-NS can again be seen equal to that between FLM-SDEu and FLM-Eu. An exception is given for the LE region, where the former deviates less. Characteristically, the inviscid methods compute an LEV-induced upper-surface c_p^0 peak instead of the viscous-observed suction plateau. This results from a separation mechanism driven by numerical viscosity instead of a physical one. Furthermore, the discontinuous c_p^0 recompression is predicted farther downstream by the inviscid methods. Both the LEV-induced $\text{Re}c_p^1$ and $\text{Im}c_p^1$ peak emerge closer to the LE, as well as more pronounced. In this regard, the experimental data is better reproduced by the inviscid methods, which is surprising. Neither FLM-SD.NS/FLM-NS nor FLM-SDEu/FLM-Eu, however, are able to render the measured $\text{Im}c_p^1$ peak at the shock location of the outer-span station.

Considering the computed global load coefficients (Table 4), FLM-SD.NS-predicted c_L^0 equals its FLM-NS counterpart, while $\text{Re}c_L^1$ is merely 3% higher. $\text{Im}c_L^1$, on the other hand, deviates by half an order of magnitude. The minuteness of either $\text{Im}c_L^1$ in comparison to the correspondent $\text{Re}c_L^1$, however, makes this circumstance again tolerable. Both computations still indicate a time-dependent c_L that minimally lags the excitation. The deviation itself can be made attributable to the differing upper-surface $\text{Im}c_p^1$ predictions in the

Table 4 Comparison of the global load coefficients for NCDW case 90D29 ($Ma_\infty = 0.90$, $Re_\infty = 10.0 \times 10^6$, $\breve{\bar{\alpha}} = 3.97$ deg, $\hat{\bar{\alpha}} = 0.5$ deg, $k_{\text{red}} = 0.240$, $x_p/c_r = 0.65$)

Method	c_L^0	$\text{Re}c_L^1$	$\text{Im}c_L^1$	$\lvert c_L^1\rvert$	$\breve{\varphi}_{c_L^1}$, deg	c_M^0	$\text{Re}c_M^1$	$\text{Im}c_M^1$	$\lvert c_M^1\rvert$	$\breve{\varphi}_{c_M^1}$, deg
FLM-SD.NS	0.263	4.065	−0.180	4.069	−2.53	0.030	0.335	−0.178	0.380	−28.02
FLM-NS	0.263	3.958	−0.051	3.959	−0.73	0.030	0.377	−0.229	0.441	−31.27
FLM-SDEu	0.274	4.066	−0.097	4.067	−1.37	0.025	0.294	−0.192	0.351	−33.13
FLM-Eu	0.273	4.062	−0.064	4.063	−0.91	0.026	0.290	−0.221	0.364	−37.25

shock region toward the tip. Disregarding viscosity yields a 4% higher c_L^0, while having only marginal impact on $\mathrm{Re}c_L^1$. The FLM-SDEu- and FLM-Eu-computed instances can be considered identical. Both $\mathrm{Im}c_L^1$ values fall within the range set up by the FLM-SD.NS and FLM-NS computation, their mutual deviation reducing significantly.

FLM-SD.NS-predicted c_M^0 equals its FLM-NS counterpart, while both $\mathrm{Re}c_M^1$ and $\mathrm{Im}c_M^1$ are gained lower in absolute value, respectively, by 11% and 22%. $\mathrm{Re}c_M^1$ and $\mathrm{Im}c_M^1$ are in the same order of magnitude. The time-dependent c_M clearly lags the excitation, indicating a damping effect on the free pitching oscillation. The deviation between the FLM-SD.NS-computed c_M^1 and its FLM-NS counterpart are attributable to the higher-order harmonics identified in the FLM-NS-computed upper-surface c_p. Their influence follows through to the time-dependent c_M evolution from which c_M^1 is extracted. FLM-SDEu- and FLM-Eu-computed c_M^0 ($\mathrm{Re}c_M^1$) are, respectively, 17% (12%) and 13% (23%) lower than their viscous counterparts. For c_M^0 the deviation experienced between the inviscid methods is 4%, an order of magnitude greater than that of c_L^0. The $\mathrm{Re}c_M^1$ instances can again be considered identical. Disregarding viscosity has only limited impact on $\mathrm{Im}c_M^1$ and thus on the degree of dynamic stability, both values again falling within the range of the FLM-SD.NS and FLM-NS computation. Their mutual deviation, however, reduces to 13%.

Overall, FLM-SD.NS renders the unsteady loading of the medium-strength shock/LEV case in satisfactory agreement to FLM-NS. For either method, the viscous consideration mainly improves on the global load coefficients' zeroth and real-part first harmonic, with the imaginary part being only marginally influenced.

Strong Shock Cases

For $Ma_\infty = 0.94$, $Re_\infty = 10.0 \times 10^6$, and $\breve{\alpha} = 0.0$ deg (cases 94D4-6), the FLM-NS supplied time-invariant mean flowfield exhibits a sizeable, equally developed supersonic region in proximity to the upper and lower wing surface. It extends, respectively, from the root to considerably beyond the tip, terminating with a strong shock slightly upstream of the TE (Fig. 12). The discontinuous recompression is substantial enough to induce postshock flow separation from $y/s = 0.83$ to $y/s = 0.98$. FLM-SD.NS-computed surface pressure distributions for 94D5 are composited with their FLM-NS and FLM-SDEu/FLM-Eu, and with their experimental counterparts in Fig. 13. The FLM-SD.NS result is described in the following. Upper- and lower-surface c_p^0, of course, exhibit symmetry.

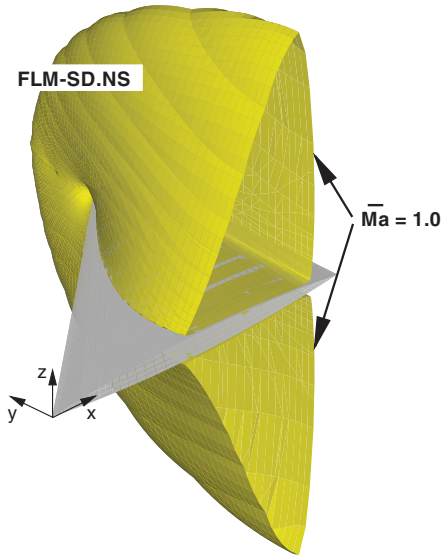

Fig. 12 Sonic isosurface of the time-invariant mean flowfield employed by FLM-SD.NS in the NCDW cases 94D4-6 ($Ma_\infty = 0.94$, $Re_\infty = 10.0 \times 10^6$, $\breve{\alpha} = 0.0$ deg, $\breve{\alpha} = 0.5$ deg, $k_{\mathrm{red}} = 0.115$, 0.230, 0.460, $x_p/c_r = 0.65$).

The onset of supersonic flow occurs significantly upstream of the obtained 90D5 locations. Correspondingly, its termination moves farther downstream, with the strong shock imposing a steep slope onto the c_p^0 progression. Again, symmetry of the upper- and lower-surface c_p^0 yields numerically nil c_L^0 and c_M^0 values. Complementary to c_p^0, upper- and lower-surface $\mathrm{Re}c_p^1$, as well as $\mathrm{Im}c_p^1$, exhibit antisymmetry. Merely considering the upper-surface distribution, the sharp LE renders an initial primary peak for both $\mathrm{Re}c_p^1$ and $\mathrm{Im}c_p^1$, respectively, being of negative and positive value. Immediately downstream, $\mathrm{Re}c_p^1$ acutely increases before merging into a positively sloped linear progression that abruptly culminates in a shock region reversal of sign. Whereas the subsequent $\mathrm{Re}c_p^1$ progression conforms to the one of 90D5 for the inner-span station, a secondary peak value emerges for the outer one. Integrating over the entire wing, both a positive $\mathrm{Re}c_L^1$ and $\mathrm{Re}c_M^1$ (pitch up) are again ascertained. The $\mathrm{Im}c_p^1$ progression exhibits the characteristics of its 90D5 counterpart, however, with strongly subdued secondary peaks being rendered in the shock region. For the inner-span station, an additional zero-crossing is observed before the shock region, reversing the secondary peak's contribution to $\mathrm{Im}c_L^1$ from positive to negative, and thus the contribution to $\mathrm{Im}c_M^1$ vice versa. Integrating over the entire wing, both a negative $\mathrm{Im}c_L^1$ and $\mathrm{Im}c_M^1$ (pitch down) are ascertained, however, each being an order of magnitude lower in absolute value than its Re counterpart.

For the investigated span stations, FLM-SD.NS-computed c_p^0, $\mathrm{Re}c_p^1$, and $\mathrm{Im}c_p^1$ agree excellently with those obtained from FLM-NS. Discrepancies are merely seen with the farther upstream prediction of the $\mathrm{Re}c_p^1$-zero crossing at the inner-span station, as well as the value of the $\mathrm{Re}c_p^1$-secondary peak at the outer-span station. For both span stations discrepancies in the $\mathrm{Im}c_p^1$-secondary peak are also noticeable. The conformity between FLM-SD.NS and FLM-NS can again be seen equal to that between FLM-SDEu and FLM-Eu. The inviscid methods, however, compute a profoundly differing behavior in the shock and postshock region. Not only is the discontinuous c_p^0 recompression predicted farther downstream, strong $\mathrm{Re}c_p^1$ and $\mathrm{Im}c_p^1$ peaks are rendered at its location, respectively, making substantial $\mathrm{Re}c_L^1$, $\mathrm{Re}c_M^1$ and $\mathrm{Im}c_L^1$, $\mathrm{Im}c_M^1$ contributions. Experimental surface pressure is best reproduced by FLM-SD.NS/FLM-NS, confirming the higher fidelity of the viscous approach.

Regarding the computed global load coefficients (Table 5), $\mathrm{Re}c_L^1$ obtained from FLM-SD.NS can be considered identical to its FLM-NS counterpart. $\mathrm{Im}c_L^1$, on the other hand, is predicted 17% lower in absolute value, attributable to differingly computed $\mathrm{Im}c_p^1$ in the shock region. Nevertheless, the two viscous methods conform in their prediction of a time-dependent c_L that lags the excitation by only a small margin. Both FLM-SDEu- and FLM-Eu-computed $\mathrm{Re}c_L^1$ are significantly higher than their viscous counterparts. The strong $\mathrm{Re}c_p^1$ peaks rendered in the shock region yield a large yet chordwise-localized difference between upper- and lower-surface distribution. Contributing positively, its summation over the semispan, however, is substantial enough to increase Rec_L^1 by 23% on average. This circumstance emerges even more pronounced in $\mathrm{Im}c_L^1$. Outside of the shock region, $\Delta\mathrm{Im}c_p^1$ would merely result in a minutely negative $\mathrm{Im}c_L^1$ similar to that of the viscous computations. Comparatively, the $\mathrm{Re}c_p^1$-corresponding $\mathrm{Im}c_p^1$ peaks contribute strongly negative to $\mathrm{Im}c_L^1$. Supplying the bulk of its value, a fourfold amplification of the viscously obtained $\mathrm{Im}c_L^1$ is experienced. The deviation between FLM-SDEu- and FLM-Eu-computed $\mathrm{Re}c_L^1$, as well as $\mathrm{Im}c_L^1$, becomes similar to that of the respective FLM-SD.NS and FLM-NS counterparts.

FLM-SD.NS predicts both $\mathrm{Re}c_M^1$ and $\mathrm{Im}c_M^1$ within 10% of the FLM-NS-gained value, the two being separated by merely half an order of magnitude. Even though $\mathrm{Re}c_L^1$ has been established as identical between the two methods, the same cannot be said for $\mathrm{Re}c_M^1$. Inversely, the deviation exhibited by $\mathrm{Im}c_L^1$ does not entirely follow through to $\mathrm{Im}c_M^1$. Considering skin friction contribution to be negligible, deviations in $\mathrm{Re}c_p^1$ are apparently amplified toward $\mathrm{Re}c_M^1$, while deviations in $\mathrm{Im}c_p^1$ are compensated toward $\mathrm{Im}c_M^1$, for the given reference axis. Both viscous methods predict the

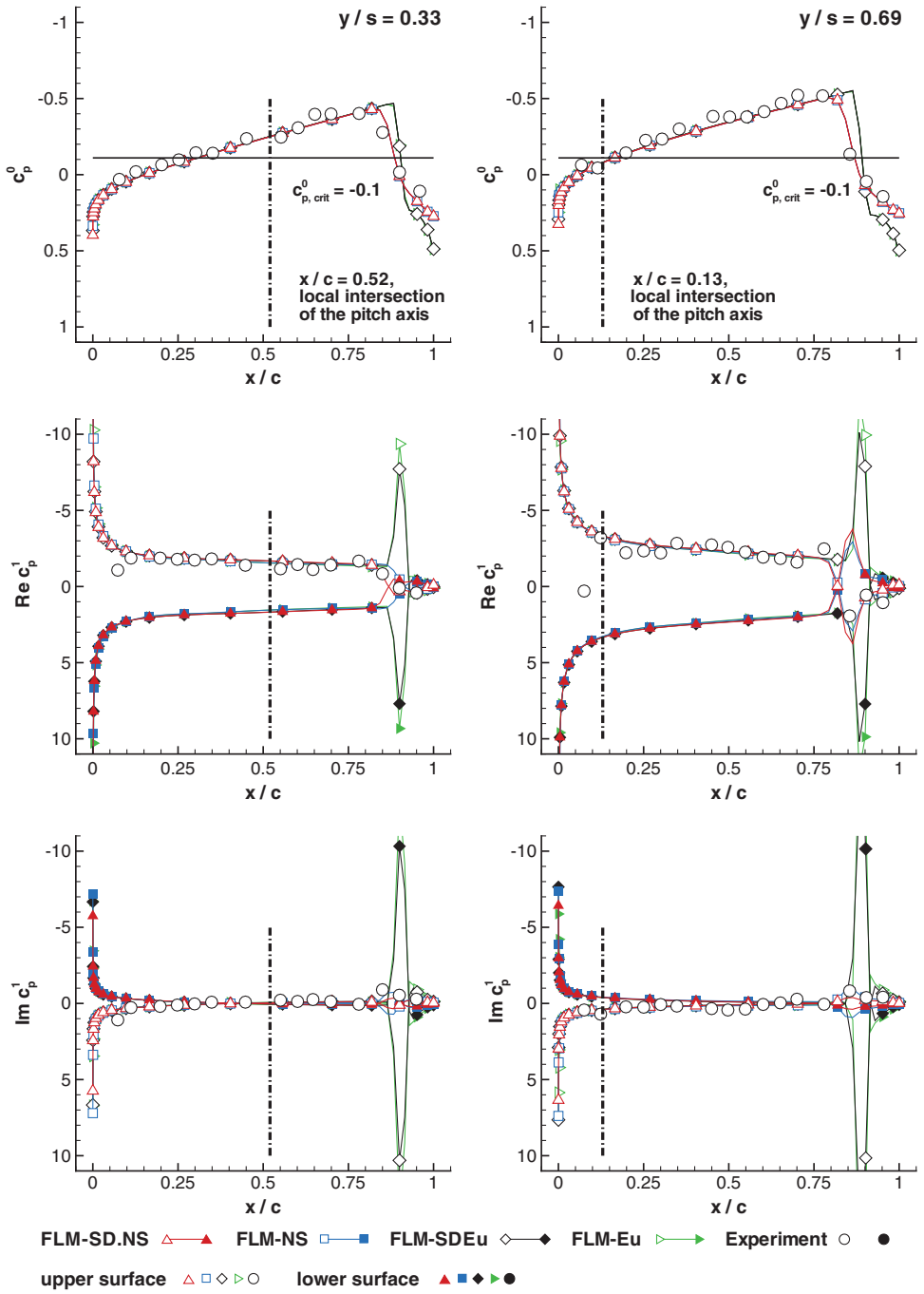

Fig. 13 Comparison of the zeroth- and first-harmonic pressure coefficient distributions (c_p^0 and c_p^1) for the NCDW case 94D5 ($Ma_\infty = 0.94$, $Re_\infty = 10.0 \times 10^6$, $\breve{\alpha} = 0.0$ deg, $\hat{\breve{\alpha}} = 0.5$ deg, $k_{red} = 0.230$, $x_p/c_r = 0.65$).

time-dependent c_M to distinctly lag the excitation, with the $\breve{\varphi}_{c_M^1}$ instances differing by merely 2%.

Disregarding viscosity, the character of c_M becomes significantly altered. FLM-SDEu-/FLM-Eu-computed $\mathrm{Re}c_M^1$ and $\mathrm{Im}c_M^1$ exchange sign as well as order of magnitude given by their viscous counterparts. Through accounted leverage, the inviscidly predicted $\mathrm{Re}c_p^1$ and $\mathrm{Im}c_p^1$ peaks in the shock region, respectively, supply the bulk negative and positive contribution that tip the scale. With $\mathrm{Im}c_M^1 > 0$ the time-dependent c_M now substantially leads the excitation. In case of a free pitching oscillation this would have an amplifying effect. For both $\mathrm{Re}c_M^1$ and $\mathrm{Im}c_M^1$ deviation between the FLM-SDEu and FLM-Eu-computed instance is within 20%, double the one exhibited

Table 5 Comparison of the global load coefficients for NCDW case 94D5 ($Ma_\infty = 0.94$, $Re_\infty = 10.0 \times 10^6$, $\breve{\alpha} = 0.0$ deg, $\hat{\breve{\alpha}} = 0.5$ deg, $k_{red} = 0.230$, $x_p/c_r = 0.65$)

Method	c_L^0	$\mathrm{Re}c_L^1$	$\mathrm{Im}c_L^1$	$\lvert c_L^1\rvert$	$\breve{\varphi}_{c_L^1}$, deg	c_M^0	$\mathrm{Re}c_M^1$	$\mathrm{Im}c_M^1$	$\lvert c_M^1\rvert$	$\breve{\varphi}_{c_M^1}$, deg
FLM-SD.NS	0.000	3.301	−0.181	3.306	−3.13	0.000	0.311	−0.077	0.321	−13.87
FLM-NS	0.000	3.302	−0.218	3.309	−3.77	0.000	0.284	−0.072	0.293	−14.18
FLM-SDEu	0.000	4.087	−0.808	4.166	−11.19	0.000	−0.016	0.197	0.198	96.61
FLM-Eu	0.000	4.034	−0.947	4.144	−13.21	0.000	−0.019	0.254	0.255	94.37

Table 6 Comparison of the global load coefficients for NCDW case 94D4 ($Ma_\infty = 0.94$, $Re_\infty = 10.0 \times 10^6$, $\breve{\alpha} = 0.0$ deg, $\hat{\breve{\alpha}} = 0.5$ deg, $k_{\text{red}} = 0.115$, $x_p/c_r = 0.65$)

Method	c_L^0	$\text{Re}c_L^1$	$\text{Im}c_L^1$	$\lvert c_L^1\rvert$	$\breve{\varphi}_{c_L^1}$, deg	c_M^0	$\text{Re}c_M^1$	$\text{Im}c_M^1$	$\lvert c_M^1\rvert$	$\breve{\varphi}_{c_M^1}$, deg
FLM-SD.NS	0.000	3.462	−0.135	3.465	−2.23	0.000	0.305	−0.052	0.309	−9.76
FLM-NS	0.000	3.483	−0.118	3.485	−1.94	0.000	0.300	−0.073	0.308	−13.71
FLM-SDEu	0.000	4.711	−0.661	4.757	−7.98	0.000	−0.219	0.157	0.269	144.46
FLM-Eu	0.000	4.754	−0.704	4.806	−8.43	0.000	−0.235	0.158	0.283	146.16

Table 7 Comparison of the global load coefficients for NCDW case 94D6 ($Ma_\infty = 0.94$, $Re_\infty = 10.0 \times 10^6$, $\breve{\alpha} = 0.0$ deg, $\hat{\breve{\alpha}} = 0.5$ deg, $k_{\text{red}} = 0.460$, $x_p/c_r = 0.65$)

Method	c_L^0	$\text{Re}c_L^1$	$\text{Im}c_L^1$	$\lvert c_L^1\rvert$	$\breve{\varphi}_{c_L^1}$, deg	c_M^0	$\text{Re}c_M^1$	$\text{Im}c_M^1$	$\lvert c_M^1\rvert$	$\breve{\varphi}_{c_M^1}$, deg
FLM-SD.NS	0.000	3.113	−0.007	3.113	−0.14	0.000	0.350	−0.208	0.407	−30.75
FLM-NS	0.000	3.123	−0.084	3.124	−1.55	0.000	0.330	−0.198	0.385	−30.87
FLM-SDEu	0.000	3.614	−0.387	3.634	−6.12	0.000	0.151	−0.050	0.159	−18.35
FLM-Eu	0.000	3.585	−0.462	3.615	−7.34	0.000	0.143	−0.038	0.148	−14.95

between the viscous counterparts. Whereas this appears reasonable for $\text{Re}c_M^1$ on grounds of its minuteness, it seems surprisingly high for $\text{Im}c_M^1$. The deviation compensates itself in the phase shift of the time-dependent c_M yet persists in its magnitude.

Retaining the freestream conditions, as well as the time-invariant mean and amplitude incidence angle of 94D5, test cases 94D4 and 94D6 embody pitching oscillations, respectively, at half and double the frequency. For both the viscous and inviscid small disturbance computations the associated time-invariant mean flowfield is, by definition, frequency independent. Therefore, they use the same particular steady-state reference-grid solution as employed in the 94D5 case. Likewise, each solution again serves as the initialization flowfield to the transient process of the correspondent dynamically fully nonlinear computation. The effects of the frequency variation on magnitude and phase angle of the global load coefficients are discussed in the following. Test case 94D4 (Table 6) is regarded first. Obtained from FLM-SD.NS, $|c_L^1|$ can be considered identical to its FLM-NS counterpart, with both methods similarly predicting a time-dependent c_L that marginally lags the excitation. In comparison with 94D5, $|c_L^1|$ is merely 5% higher, with the lagging phase angle having decreased only slightly. FLM-SDEu- and FLM-Eu-computed $|c_L^1|$ can also be considered identical to one another, with the $\breve{\varphi}_{c_L^1}$ instances differing by a mere 5%. The inviscidly computed $|c_L^1|$ is about 38% higher than its viscous counterpart, with the lag of the time-dependent c_L having increased as well. Both $\breve{\varphi}_{c_L^1}$ instances, however, remain in the single-digit degree range. At half the 94D5 frequency, the inviscidly computed $|c_L^1|$ presents itself about 15% higher, whereas the lagging phase angle has decreased from the low double-digit to the single-digit degree range.

Obtained from FLM-SD.NS, $|c_M^1|$ can be considered identical to its FLM-NS counterpart, with both methods predicting a time-dependent c_M that lags the excitation. Either $\breve{\varphi}_{c_M^1}$ instance presents itself in the low double-digit degree range, with FLM-SD.NS indicating a slightly lesser degree of dynamic stability for the free pitching oscillation than FLM-NS. Whereas the $|c_M^1|$ instances can be considered equal to the mean of their 94D5 counterparts, the mean of the $\breve{\varphi}_{c_M^1}$ instances has decreased somewhat in absolute value. Obtained from FLM-SDEu, $|c_M^1|$ is merely 5% lower than its FLM-Eu counterpart, with the $\breve{\varphi}_{c_M^1}$ instances being nearly equal. The mean of the inviscidly computed $|c_M^1|$ instances is 11% lower than its viscous counterpart. Similar to 94D5, disregarded viscosity renders a time-dependent c_M that leads the excitation, which in case of a free pitching oscillation would have an amplifying effect. At half the 94D5 frequency, however, the mean of the FLM-SDEu- and FLM-Eu-computed $|c_M^1|$ instances has gained 22%, while its phase lag has increased to slightly more than three-eighths of a cycle. Notably, the reduction of frequency has had a substantial impact on the inviscid time-dependent c_M, where it only has had a marginal one on the viscous counterpart.

Regarding 94D6 (Table 7), $|c_L^1|$ obtained from FLM-SD.NS can be considered identical to its FLM-NS counterpart, with both methods predicting a time-dependent c_L that marginally lags the excitation. The FLM-SD.NS prediction may even be perceived as being entirely in phase. $|c_L^1|$ is merely 6% lower than in 94D5, with the phase lag having decreased slightly. FLM-SDEu- and FLM-Eu-computed $|c_L^1|$ can also be considered identical, with the $\breve{\varphi}_{c_L^1}$ instances conforming well. The inviscidly computed $|c_L^1|$ is about 16% higher than its viscous counterpart, with the lag of the time-dependent c_L having increased too. Both inviscidly computed $\breve{\varphi}_{c_L^1}$ instances, however, remain in the single-digit degree range. At double the 94D5 frequency, $|c_L^1|$ presents itself 13% lower, with the lagging phase angle having decreased from the low double-digit to the single-digit degree range.

FLM-SD.NS predicts $|c_M^1|$ within 6% of the FLM-NS-gained value, while the obtained instances of $\breve{\varphi}_{c_M^1}$ can be considered identical. At double the 94D5 frequency, the mean of the FLM-SD.NS- and FLM-NS- computed $|c_M^1|$ has increased by 29%. The time-dependent c_M now lags the excitation even more distinctly, indicating a substantially higher degree of dynamic stability for the free pitching oscillation. The deviation between the FLM-SDEu- and FLM-Eu-computed $|c_M^1|$ instances is similar to the one witnessed between the FLM-SD.NS- and FLM-NS-computed counterparts, whereas a greater variation can be observed for $\breve{\varphi}_{c_M^1}$. Disregarding viscosity entails a 61% lower mean $|c_M^1|$ and a 46% lower mean lagging phase angle, the latter indicating a lesser degree of dynamic stability for the free pitching oscillation. From 94D5 to 94D6, the mean of the inviscidly computed $|c_M^1|$ instances has decreased by 32%. Even more notably, a reversal in sign has occurred for $\breve{\varphi}_{c_M^1}$, toward the higher frequency. Whereas the time-dependent c_M leads the excitation by slightly more than a quarter cycle for 94D5, it distinctly lags the excitation for 94D6. In the case of a free pitching oscillation, c_M goes from having an amplifying to a damping effect, the latter now conforming to the FLM-SD.NS/FLM-NS prediction.

Overall, FLM-SD.NS renders the unsteady loading of the strong shock cases 94D4-6 in good agreement to FLM-NS. For either method, the viscous consideration yields a substantial improvement over the associated inviscid approach. The more-complete flow model contrarily indicates dynamic stability for both 94D4 and 94D5.

Computational Efficiency

FLM-SD.NS and FLM-NS computation times, as well as the inverse ratio between the two, are summarized in Table 8. Evidently, FLM-SD.NS realizes reductions up to an order of magnitude. Whereas $\breve{t}_{\text{CPU}}^{\text{SD.NS}}$ are all within 24 h, a far greater range can be observed for $\breve{t}_{\text{CPU}}^{\text{NS}}$, the computation of 90D5 and 94D4-6 taking longer than 90D29 by multiples. At default settings, the dynamically fully

Table 8 Quantitative comparison of computational effort between FLM-SD.NS and FLM-NS for all NCDW cases, as well as between FLM-SDEu and FLM-Eu for 94D4-6 ($Ma_\infty = 0.94$, $Re_\infty = 10.0 \times 10^6$, $\breve{\bar{\alpha}} = 0.0$ deg, $\breve{\dot{\alpha}} = 0.5$ deg, $k_{red} = 0.115$, 0.230, 0.460, $x_p/c_r = 0.65$)

Case	$\breve{t}^{SD.NS}_{CPU}$, h	$\breve{t}^{NS}_{CPU}$, h	ζ_{CPU}	$\breve{t}^{SDEu}_{CPU}$, h	$\breve{t}^{Eu}_{CPU}$, h	ζ_{CPU}
90D5 [a]	24.1	419.8	17.4	n/a	n/a	n/a
90D29 [a]	21.2	71.3	3.4	n/a	n/a	n/a
94D4 [b]	16.9	261.0	15.4	3.4	88.3	26.0
94D5 [b]	17.2	242.7	14.1	3.2	78.8	24.6
94D6 [b]	26.4	216.8	8.2	3.7	71.1	19.2

[a]Conducted on a single 1.3 GHz Intel Itanium 2 processor
[b]Conducted on a single 1.6 GHz Intel Itanium 2 processor

nonlinear treatment of the $\breve{\bar{\alpha}} = 0$ deg incidence motion had exhibited solution instabilities toward the upper/lower dead center; that is, at physical time steps where the deflected wing experiences strong deceleration and acceleration. Merely very high instances of implicit damping allowed for a remedy, significantly drawing out the computation in turn. Compared to 90D5, the reduced ζ_{CPU} witnessed for 94D5 stems in part from the employed higher-clocking processor, accelerating FLM-NS considerably more than FLM-SD.NS. The frequency variation conducted on the basis of 94D5 further reveals an increase of $\breve{t}^{SD.NS}_{CPU}$ by 56% from 94D4 to 94D6, with a decrease of $\breve{t}^{NS}_{CPU}$ by 17% occurring correspondingly. This opposing tendency results in a 47% reduction of ζ_{CPU} across the considered spectrum. Vice versa, it can be said that a 75% decrease of the 94D6 frequency leads to a twofold increase of FLM-SD.NS performance over FLM-NS, qualitatively confirming a trait already experienced in the investigated airfoil cases [13]. With 1.7 GB of RAM, FLM-SD.NS allocates four times more working memory than FLM-NS, as both complex amplitude and time-invariant mean entities need to be stored. It is the tradeoff made toward superior computational efficiency.

Unlike 90D5 and 90D29, the 94D4-6 FLM-SDEu and FLM-Eu computations were conducted on the same processor, just as used by FLM-SD.NS and FLM-NS before. Thus, a comparison of $\breve{t}^{SDEu}_{CPU}$ with $\breve{t}^{Eu}_{CPU}$, as well as each instance with its respective viscous counterpart becomes possible. Likewise compiled in Table 8, $\breve{t}^{SDEu}_{CPU}$ is on average 83% lower than $\breve{t}^{SD.NS}_{CPU}$, while merely increasing by 9% from 94D4 to 94D6. In contrast, $\breve{t}^{Eu}_{CPU}$ (an invariant 66% lower than $\breve{t}^{NS}_{CPU}$) decreases by 20%, a range approximately equal to the one observed for $\breve{t}^{NS}_{CPU}$. Apparently, the opposing tendency witnessed between $\breve{t}^{SD.NS}_{CPU}$ and t^{NS}_{CPU} over the spectrum already exists between $\breve{t}^{SDEu}_{CPU}$ and t^{Eu}_{CPU}; that is,

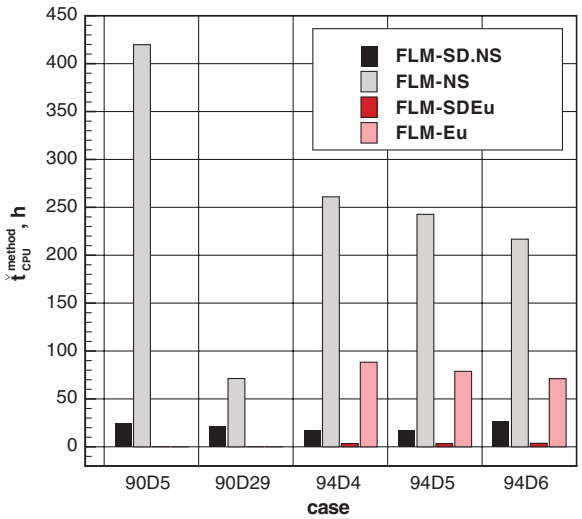

Fig. 14 Qualitative comparison of computational effort between FLM-SD.NS and FLM-NS for all NCDW cases, as well as between FLM-SDEu and FLM-Eu for 94D4-6 ($Ma_\infty = 0.94$, $Re_\infty = 10.0 \times 10^6$, $\breve{\bar{\alpha}} = 0.0$ deg, $\breve{\dot{\alpha}} = 0.5$ deg, $k_{red} = 0.115$, 0.230, 0.460, $x_p/c_r = 0.65$).

Table 9 Specifications of the employed computational grids

	Embedding volume		Wing surface	
Grid pair	Extent	Cells	Extent	Cells
Coarse	$2 \times (48 \times 24 \times 20)$	46,080	$2 \times (36 \times 16)$	1,152
Baseline	$2 \times (96 \times 48 \times 40)$	368,640	$2 \times (72 \times 32)$	4,608
Fine	$2 \times (104 \times 56 \times 48)$	559,104	$2 \times (72 \times 32)$	4,608

for the computations with the reduced flow model. From 94D4 to 94D6, ζ_{CPU} diminishes by 26%, far less than observed in the viscous treatment. On average, ζ_{CPU} of FLM-SD.NS/FLM-NS is half that of FLM-SDEu/FLM-Eu, indicating a relative loss of computational efficiency improvement toward the more complete flow model's implementation. With 1.3 GB of RAM, FLM-SDEu allocates four times more working memory than FLM-Eu. As FLM-SD.NS scales equally to FLM-NS, no relative penalty can be said to have occurred in its resource need. Supplementally, the comparison of computation times is visualized in Fig. 14.

Grid Sensitivity

Investigating the independence of the FLM-SD.NS computation from the employed grid pair, both a coarser and finer instance of the already used extremum and reference grid (henceforth referred to as the baseline-grid pair) are taken into account (Table 9). Whereas the coarse-grid pair is equal to the one employed in the 90D29 FLM-SDEu/FLM-Eu comparative computation, the fine-grid pair was specifically generated for this purpose. It retains the baseline-grid pair's topology and far-field distances, as well as the inherent wing's surface discretization. The delimited volume, on the other hand, is newly discretized with 104 cells in positive chordwise, 56 cells in spanwise (the first 32 defining the wing), and 48 cells in wing surface normal direction, per block. The 559,104 volume cells represent a 52% increase respective of the baseline, with the number of cells in wing normal direction having risen by 20%. These are again hyperbolically distributed, the distance of the first offbody grid plane remaining set at $1 \times 10^{-5} \times s$. Both extremum and reference grid are elliptically smoothed [22]. Eventually, FLM-SD.NS computations of test cases 90D5, 90D29, and 94D5, conducted with the coarse- and fine-grid pairs, supplement those already presented (the baseline). Grid sensitivity is assessed by means of the global load coefficients' variation.

Regarding 90D5 (Table 10), the computation with the coarse-grid pair yields a c^0_L that can again be considered numerically nil and thus invariant to the baseline value. While $\mathrm{Re}c^1_L$ is merely 3% higher, coarse and baseline $\mathrm{Im}c^1_L$ are separated by nearly an order of magnitude, the former being greater in absolute value. For the computation on the fine-grid pair, both c^0_L and $\mathrm{Re}c^1_L$ are observed to be identical to the respective baseline value. $\mathrm{Im}c^1_L$, however, is half an order of magnitude lower in absolute value than its baseline counterpart, revealing a time-dependent c_L approximately in phase with the excitation. Overall, $\mathrm{Im}c^1_L$ reacts substantially to the grid variation, whereas $\mathrm{Re}c^1_L$ does not (a sensitivity rooted in the minuteness of the former with respect to the latter). Coarse c^0_M can again be considered numerically nil and thus invariant to the baseline value. In this regard, $\mathrm{Re}c^1_M$ and $\mathrm{Im}c^1_M$ are, respectively, 27% and 21% lower in absolute value than the particular baseline counterpart. On the other hand, the fine-grid computation yields an identical c^0_M, a $\mathrm{Re}c^1_M$ higher by merely 2%, as well as an identical $\mathrm{Im}c^1_M$; that is, all evidently converging with those obtained from the baseline-grid pair. Notably, the sensitivity exhibited by $\mathrm{Im}c^1_L$ between these two grid pairs has not followed through to $\mathrm{Im}c^1_M$. For 90D5 the baseline-grid pair is deemed to have sufficiently resolved the global load coefficients.

In regard to 90D29 (Table 11), it proved futile to achieve a stable FLM-SD.NS solution with the coarser grid pair, even though a time-invariant mean flowfield had been realized with FLM-NS in the reference grid. Therefore, only c^0_L and c^0_M are available for comparison. They are 3 and 7% lower, respectively, than their particular baseline counterpart. For the computation on the fine-grid

Table 10 Grid influence on the FLM-SD.NS-computed global load coefficients of NCDW case 90D5 ($Ma_\infty = 0.90, Re_\infty = 10.0 \times 10^6, \breve{\alpha} = 0.0$ deg, $\hat{\alpha} = 0.5$ deg, $k_{red} = 0.237, x_p/c_r = 0.65$)

Grid pair	c_L^0	$\mathrm{Re}c_L^1$	$\mathrm{Im}c_L^1$	$\lvert c_L^1\rvert$	$\breve{\varphi}_{c_L^1}$, deg	c_M^0	$\mathrm{Re}c_M^1$	$\mathrm{Im}c_M^1$	$\lvert c_M^1\rvert$	$\breve{\varphi}_{c_M^1}$, deg
Coarse	0.000	3.850	−0.094	3.851	−1.40	0.000	0.235	−0.140	0.274	−30.80
Baseline	0.000	3.748	−0.013	3.748	−0.20	0.000	0.322	−0.178	0.368	−28.87
Fine	0.000	3.733	−0.003	3.733	−0.04	0.000	0.328	−0.180	0.374	−28.72

Table 11 Grid influence on the FLM-SD.NS-computed global load coefficients of NCDW case 90D29 ($Ma_\infty = 0.90, Re_\infty = 10.0 \times 10^6, \breve{\alpha} = 3.97$ deg, $\hat{\alpha} = 0.5$ deg, $k_{red} = 0.240, x_p/c_r = 0.65$)

Grid pair	c_L^0	$\mathrm{Re}c_L^1$	$\mathrm{Im}c_L^1$	$\lvert c_L^1\rvert$	$\breve{\varphi}_{c_L^1}$, deg	c_M^0	$\mathrm{Re}c_M^1$	$\mathrm{Im}c_M^1$	$\lvert c_M^1\rvert$	$\breve{\varphi}_{c_M^1}$, deg
Coarse	0.256	n/a	n/a	n/a	n/a	0.028	n/a	n/a	n/a	n/a
Baseline	0.263	4.065	−0.180	4.069	−2.53	0.030	0.335	−0.178	0.380	−28.02
Fine	0.261	4.087	−0.183	4.091	−2.57	0.031	0.335	−0.180	0.381	−28.30

Table 12 Grid influence on the FLM-SD.NS-computed global load coefficients of NCDW case 94D5 ($Ma_\infty = 0.94, Re_\infty = 10.0 \times 10^6, \breve{\alpha} = 0.0$ deg, $\hat{\alpha} = 0.5$ deg, $k_{red} = 0.230, x_p/c_r = 0.65$)

Grid pair	c_L^0	$\mathrm{Re}c_L^1$	$\mathrm{Im}c_L^1$	$\lvert c_L^1\rvert$	$\breve{\varphi}_{c_L^1}$, deg	c_M^0	$\mathrm{Re}c_M^1$	$\mathrm{Im}c_M^1$	$\lvert c_M^1\rvert$	$\breve{\varphi}_{c_M^1}$, deg
Coarse	0.000	3.329	−0.105	3.331	−1.81	0.000	0.281	−0.090	0.295	−17.71
Baseline	0.000	3.301	−0.181	3.306	−3.13	0.000	0.311	−0.077	0.321	−13.87
Fine	0.000	3.359	−0.214	3.366	−3.64	0.000	0.287	−0.069	0.295	−13.47

pair, both c_L^0 and $\mathrm{Re}c_L^1$ are observed to be identical to the respective baseline value, with $\mathrm{Im}c_L^1$ merely being 2% higher in absolute value. A similar increase is witnessed for c_M^0 (three percent), with both $\mathrm{Re}c_M^1$ and $\mathrm{Im}c_M^1$ observed to be identical to their particular baseline value. Thus, the baseline-grid pair is considered to have sufficiently resolved the global load coefficients.

Finally focusing on 94D5 (Table 12), the computation with the coarse-grid pair yields a c_L^0 that can again be considered numerically nil and thus invariant to the baseline value. While $\mathrm{Re}c_L^1$ is observed to be identical, coarse and baseline $\mathrm{Im}c_L^1$ are separated by a factor of nearly two, the former being lower in absolute value. For the computation with the fine-grid pair, c_L^0 remains identical, with $\mathrm{Re}c_L^1$ being only 2% higher than its baseline counterpart. $\mathrm{Im}c_L^1$, however, is 18% higher in absolute value, a deviation that compensates itself in the magnitude of the time-dependent c_L yet persists in the phase angle. Again, a sensitivity of $\mathrm{Im}c_L^1$ to the grid pair variation can be established yet not witnessed as severe as in 90D5, due to it merely being an order of magnitude removed from $\mathrm{Re}c_L^1$. Coarse c_M^0 can again be considered numerically nil and thus invariant to the baseline value. In this regard, $\mathrm{Re}c_M^1$ is gained 10% lower and $\mathrm{Im}c_M^1$ 17% higher in absolute value than the particular baseline counterpart. The fine-grid computation yields an identical c_M^0, while both $\mathrm{Re}c_M^1$ and $\mathrm{Im}c_M^1$ deviate by up to 10%. This instance follows through to the magnitude of the time-dependent c_M, yet not its lagging phase angle. Nevertheless, the first harmonic of the moment coefficient has not entirely converged between the baseline and fine-grid pair, in contrast to 90D5. As discussed for the airfoil test cases of [13], the spatial discretization's influence on the FLM-SD.NS prediction is primarily a resolution issue of the FLM-NS-supplied time-invariant mean flowfield. Minor deviations already exhibited in the time-invariant mean shock's location and intensity between the baseline and fine reference grid will become amplified in the FLM-SD.NS-computed first harmonic. For 94D5, the time-invariant mean flowfield features a shock not only sufficiently stronger than for 90D5 but also extending farther into the near field from the wing's surface. Consequently, its resolution is far more susceptible to the spatial discretization than in the latter case, accounting for the coefficient's sustained deviation despite an increased number of volume cells. Since the focus of the present study has been an intermethod comparison conducted on consistent grid pairs (accomplished with exception of the 90D29 inviscid computations, which had used the coarser one), the 94D5 baseline result is still deemed acceptable. An investigation with an even finer grid pair was not conducted.

In regard to the baseline-grid pair, FLM-SD.NS computational time per pseudotime step and per cell is about 72 μs for both 90D5 and 90D29, as well as 51 μs for 94D5, the reduction being an effect of the 94D5-employed higher-clocking processor. Considering the fine- and coarse-grid pairs, the case-particular computational time per pseudotime step and per cell varies only marginally. Thus, computational time per pseudotime step itself can be said to scale as a function of the cell number.

Conclusions

In an effort to further substantiate FLM-SD.NS application readiness, computational results for NCDW harmonic pitching oscillations were presented and compared with those of FLM-NS, FLM-SDEu/FLM-Eu, as well as experimental data. A weak shock case and a strong shock case undergoing a variation in frequency demonstrated the small disturbance Navier–Stokes approach's accuracy and efficiency in predicting the unsteady local and global loading. Special attention had been given to the obtained $\mathrm{Im}c_M^1$, as it is indicative of the corresponding free oscillation's amplified or damped state. In this regard, the strong shock case illustrates the benefit of the viscous consideration, FLM-SD.NS/FLM-NS predicting dynamic stability at frequencies where FLM-SDEu/FLM-Eu does not. The medium-strength shock/LEV case, on the other hand, discloses the limitations of the small disturbance approach. Fourier analysis of the FLM-NS-computed upper-surface c_p reveals localized higher-order harmonics that are no longer negligible. They result from the LEV itself, as well as the LEV's interaction with the shock. With influence exerted on the time-dependent c_M evolution, the Fourier-analysis-obtained $\mathrm{Im}c_M^1$ and the FLM-SD.NS-computed one exhibit the most pronounced deviation among the investigated cases.

To date, more application-oriented investigations have been realized with FTDW harmonic pitching oscillations. A shockless case, an LEV case, and a medium-strength shock case were computed with FLM-SD.NS/FLM-NS, as well as FLM-SDEu/FLM-Eu. The promising results will be presented in the near future. Complementary studies for high-aspect-ratio wings and a

rectangular wing/nacelle configuration undergoing harmonic motions are on the verge of completion, while an assessment of FLM-SD.NS/FLM-SDEu prediction quality with regard to the AGARD 445.6 wing's flutter boundary has just commenced.

References

[1] Schuster, D. M., Liu, D. D., and Huttsell, L. J., "Computational Aeroelasticity: Success, Progress, Challenge," *Journal of Aircraft*, Vol. 40, No. 5, 2003, pp. 843–856. doi:10.2514/2.6875

[2] Dowell, E., Edwards, J., and Strganac, T., "Nonlinear Aeroelasticity," *Journal of Aircraft*, Vol. 40, No. 5, 2003, pp. 857–874. doi:10.2514/2.6876

[3] Clark, W. S., and Hall, K. C., "A Time-Linearized Navier–Stokes Analysis of Stall Flutter," *Journal of Turbomachinery*, Vol. 122, No. 3, 2000, pp. 467–476. doi:10.1115/1.1303073

[4] Ekici, K., Voytovych, D. M., and Hall, K. C., "Time-Linearized Navier–Stokes Analysis of Flutter in Multistage Turbomachines," AIAA Paper 2005-836, Jan. 2005.

[5] Campobasso, M. S., and Giles, M. B., "Effects of Flow Instabilities on the Linear Analysis of Turbomachinery Aeroelasticity," *Journal of Propulsion and Power*, Vol. 19, No. 2, 2003, pp. 250–259. doi:10.2514/2.6106

[6] Campobasso, M. S., and Giles, M. B., "Stabilization of Linear Flow Solver for Turbomachinery Aeroelasticity Using Recursive Projection Method," *AIAA Journal*, Vol. 42, No. 9, 2004, pp. 1765–1774. doi:10.2514/1.1225

[7] Chassaing, J. C., and Gerolymos, G. A., "Time-Linearized Time-Harmonic 3D Navier–Stokes Shock-Capturing Schemes," *International Journal for Numerical Methods in Fluids*, Vol. 56, No. 3, 2008, pp. 279–303. doi:10.1002/fld.1523

[8] Spalart, P. R., and Allmaras, S. R., "A One-Equation Turbulence Model for Aerodynamic Flows," AIAA Paper 92-0439, Jan. 1992.

[9] Petrie-Repar, P., "Development of an Efficient and Robust Linearised Navier–Stokes Flow Solver," *Unsteady Aerodynamics, Aeroacoustics and Aeroelasticity of Turbomachines*, edited by K. C. Hall, R. E. Kielb, and J. P. Thomas, Springer, The Netherlands, 2006, pp. 437–448.

[10] Hall, K. C., Thomas, J. P., and Clark, W. S., "Computation of Unsteady Nonlinear Flows in Cascades Using a Harmonic Balance Technique," *AIAA Journal*, Vol. 40, No. 5, 2002, pp. 879–886. doi:10.2514/2.1754

[11] Thomas, J. P., Dowell, E. H., and Hall, K. C., "Modeling Viscous Transonic Limit Cycle Oscillation Behavior Using a Harmonic Balance Technique," *Journal of Aircraft*, Vol. 41, No. 6, 2004, pp. 1266–1274. doi:10.2514/1.9839

[12] Kreiselmaier, E., and Laschka, B., "Small Disturbance Euler Equations: Efficient and Accurate Tool for Unsteady Load Predictions," *Journal of Aircraft*, Vol. 37, No. 5, 2000, pp. 770–778. doi:10.2514/2.2699

[13] Pechloff, A., and Laschka, B., "Small Disturbance Navier–Stokes Method: Efficient Tool for Predicting Unsteady Air Loads," *Journal of Aircraft*, Vol. 43, No. 1, 2006, pp. 17–29. doi:10.2514/1.14350

[14] Allen, A., Iatrou, M., Pechloff, A., and Laschka, B., "Computation of Delta Wing Flap Oscillations with a Reynolds-Averaged Navier–Stokes Solver," *New Results in Numerical and Experimental Fluid Mechanics 5: Contributions to the 14th STAB-DGLR-Symposium, Bremen, Germany 2004*, edited by H.-J. Rath, C. Holze, H.-J. Heinemann, R. Henke, and H. Hönlinger, Notes on Numerical Fluid Mechanics and Multidisciplinary Design, Vol. 92, Springer–Verlag, Berlin, 2006, pp. 85–93. doi:10.1007/978-3-540-33287-9_11

[15] Roe, P. L., "Approximate Riemann Solvers, Parameter Vectors and Difference Schemes," *Journal of Computational Physics*, Vol. 43, No. 2, 1981, pp. 357–372. doi:10.1016/0021-9991(81)90128-5

[16] Chakravarthy, S. R., "High Resolution Upwind Formulations for the Navier–Stokes Equations," *Von Kármán Institute Lecture Series on Computational Fluid Dynamics*, Von Kármán Institute, 1988-05, Brussels, March 1988, pp. 1–105.

[17] Blazek, J., "A Multigrid LU-SSOR Scheme for the Solution of Hypersonic Flow Problems," AIAA Paper 1994-0062, Jan. 1994.

[18] Whitfield, D. L., and Janus, J. M., "Three-Dimensional Unsteady Euler Equations Solution Using Flux Vector Splitting," AIAA Paper 1984-1552, June 1984.

[19] Bennett, R. M., and Walker, C. E., "Computational Test Cases for a Clipped Delta Wing with Pitching and Trailing Edge Control Surface Oscillations," NASA TM-1999-209104, 1999.

[20] Weishäupl, C., and Laschka, B., "Small Disturbance Euler Simulations for Unsteady Flows of a Delta Wing due to Harmonic Oscillations," *Journal of Aircraft*, Vol. 41, No. 4, 2004, pp. 782–789. doi:10.2514/1.12601

[21] Iatrou, M., Allen, A., Pechloff, A., Breitsamter, C., and Laschka, B., "Small Disturbance Euler/Navier–Stokes Computations for Delta Wing Flap Oscillations," *Flow-Induced Unsteady Loads and the Impact on Military Applications*, NATO Research and Technology, MP-AVT-123, Budapest, April 2005, pp. 16-1–16-2.

[22] Markmiller, J., "Validierung Eines Zeitechten und Eines Small Disturbance Navier–Stokes Verfahrens an Einem Schwingenden Deltaflügel," Diploma Thesis, Inst. for Fluid Mechanics, Technical Univ. of Munich, Rept. TUM-FLM-2003/28, Garching, Germany, Oct. 2003.